



저작자표시-비영리-변경금지 2.0 대한민국

이용자는 아래의 조건을 따르는 경우에 한하여 자유롭게

- 이 저작물을 복제, 배포, 전송, 전시, 공연 및 방송할 수 있습니다.

다음과 같은 조건을 따라야 합니다:



저작자표시. 귀하는 원저작자를 표시하여야 합니다.



비영리. 귀하는 이 저작물을 영리 목적으로 이용할 수 없습니다.



변경금지. 귀하는 이 저작물을 개작, 변형 또는 가공할 수 없습니다.

- 귀하는, 이 저작물의 재이용이나 배포의 경우, 이 저작물에 적용된 이용허락조건을 명확하게 나타내어야 합니다.
- 저작권자로부터 별도의 허가를 받으면 이러한 조건들은 적용되지 않습니다.

저작권법에 따른 이용자의 권리는 위의 내용에 의하여 영향을 받지 않습니다.

이것은 [이용허락규약\(Legal Code\)](#)을 이해하기 쉽게 요약한 것입니다.

[Disclaimer](#)

재료공학 박사학위논문

Ab-initio study on optical and electrical properties of
oxide semiconductors

산화물 반도체의 광학 및 전기적 성질에 관한
제일원리 계산 연구

2015년 7월

서울대학교 대학원

공과대학 재료공학부

강영호

Abstract

Ab-initio study on optical and electrical properties of oxide semiconductors

Youngho Kang

Department of Materials Science and Engineering

The Graduate School

Seoul National University

Oxide semiconductor (OS) is a promising candidate for the application to large-area and flexible opto-electrical devices, because OS which is deposited at low temperature exhibits the outstanding electrical properties showing the high electron mobility ($\sim 10 \text{ cm}^2/\text{Vs}$) in comparison with the widely used semiconductors such as amorphous Si (*a*-Si). In addition, since OS is transparent in the most visible and near-infrared regions due to their large band gap, it is often called transparent oxide semiconductor and can be expected to offer a solution for fabrication of the transparent electronic device on flexible substrates. In spite of the advantages of OS, previous experimental studies reported various obstacles to be overcome for realization of the device utilizing OSs. For example, the OS based thin film transistor (TFT) suffers from device instabilities under illumination and bias stress. In addition, the underlying mechanism for the charge transport in OS still remains unclear, which hinders improvement of the OS based device performance.

In this research, we investigate the optical and electrical properties of OSs using *ab-initio* calculations on the basis of density functional theory (DFT) to suggest the strategy to improve the performance of OSs in terms of electron transport and reliability. First, in order to investigate the electron transport in OSs, we introduce

the model Hamiltonian for the conduction band within tight-binding approximation and carry out the calculation of the electron mobility considering several types of scattering processes. It is found that the interaction between metal s and oxygen p orbitals under tetrahedral and octahedral local atomic structure gives the quasi-linear dispersion of the conduction band which plays an important role in determining the electron mobility in OSs. In addition, we reveal that the electron mobility in a multi-component OS like InGaZnO_4 is dominated by the cation-disorder scattering process.

Next, we investigate the influence of hydrogen impurity in OS. Previously, various models to explain the threshold voltage shifts under illumination and bias stress were suggested based on oxygen vacancy defect, but the clear mechanisms for that are still controversial. In this study, the DFT calculation results turn out that hydrogen in OSs can have $+1/-1$ charge state depending on Fermi level. This bistability of hydrogen enables to cause the threshold voltage shift by alternating its charge state under illumination and bias stress.

In a second part, the optical properties are mainly dealt with. For the more realistic modelling, we study the *ab-initio* calculation methodology based on GW approximation for obtaining the accurate band gap of OS. The DFT calculation usually results in 30~40% underestimation of the band gap in typical insulator and GW method improves the accuracy of the calculated band gap by correcting exchange-correlation energy of the conventional DFT calculation. However, previous GW calculation results for OSs still yield ~10% lower band gap than experimental value. Thus, we investigate the theoretical reason for such wrong description of GW method for OSs and suggest new method to further improve the predictive power of GW method, which shows the mean absolute relative error (MARE) of ~3%.

Finally, we study the visible light absorption of amorphous In-Ga-Zn-O since the device degradation critically occurs when exposed to visible and UV light. It is found that the relative downshift of the conduction band position comparing to that of crystalline phase occurs as well as long tail states near the valence band

edge appear in amorphous phase. This is one of the main reasons for amorphous OSs to absorb the visible light without any defects.

Keywords : oxide semiconductors, density functional theory (DFT), electron transport, point defect, light absorption

Student Number : 2011-20616

| | |
|--|-----------|
| Abstract | |
| Contents | |
| List of table and figures | |
| 1. Introduction | 1 |
| 1.1 Overview of oxide semiconductor (OS) | 1 |
| 1.2 Challenges in utilization of OS | 6 |
| 1.2.1 Transport mechanisms in OS | 6 |
| 1.2.2 Degradation phenomena in OS device | 10 |
| 1.3 Goal of the dissertation | 13 |
| 1.4 Organization of the dissertation | 17 |
| 1.5 Bibliography | 18 |
| 2. Theoretical background | 20 |
| 2.1 Density functional theory (DFT) | 20 |
| 2.1.1 Hohenberg and Kohn theorem | 20 |
| 2.1.2 Kohn-Sham equation | 23 |
| 2.2 Exchange-correlation energy | 26 |
| 2.2.1 Local density approximation (LDA) | 26 |
| 2.2.2 Generalized gradient approximation (GGA) | 29 |
| 2.3 Beyond the DFT | 31 |
| 2.3.1 DFT+ U | 31 |
| 2.3.2 Hybrid functional | 33 |
| 2.3.3 GW approximation | 37 |
| 2.4 Electron transport | 40 |

| | |
|--|------------|
| 2.4.1 Fermi-Golden rule | 40 |
| 2.4.2 Boltzmann transport equation | 43 |
| 2.5 Optical absorption in insulator | 45 |
| 2.6 Defect formation energy | 47 |
| 2.7 Bibliography | 49 |
| 3. Electronic property of OS | 50 |
| 3.1 Introduction | 50 |
| 3.2 Calculation method | 51 |
| 3.3 Results and discussion | 54 |
| 3.3.1 Quasi-linear band structures in OS | 54 |
| 3.3.2 Electron mobility in crystalline ZnO | 65 |
| 3.3.3 Electron mobility in crystalline In-Ga-Zn-O (IGZO) | 68 |
| 3.3.4 Hydrogen defect in In-Zn-Sn-O (IZTO) | 76 |
| 3.4 Bibliography | 86 |
| 4. Optical property of OS | 88 |
| 4.1 Introduction | 88 |
| 4.2 Calculation method | 89 |
| 4.3 Results and discussion | 93 |
| 4.3.1 Band gap of OS in GW approximation | 93 |
| 4.3.2 Optical absorption of crystalline and amorphous IGZO | 101 |
| 4.4 Bibliography | 109 |
| 5. Conclusion | 111 |
| 국문초록 | 114 |

List of table and figures

| | |
|---|----|
| Table 4.1 The quasiparticle band gaps | 98 |
| Fig. 1.1 Schematic TFT device structure | 2 |
| Fig. 1.2 Device structure of TFT using a-IGZO | 5 |
| Fig. 1.3 Electron mobility in ZnO and In ₂ O ₃ | 7 |
| Fig. 1.4 Device degradation in experiments | 11 |
| Fig. 2.1 Schematic figure for solving KS equation | 25 |
| Fig. 2.2 Diagram for the energy change of exchange-correlation functional | 28 |
| Fig. 2.3 Lattice and band gap in HSE functional | 36 |
| Fig. 3.1 Wannier functions in zincblende ZnO | 52 |
| Fig. 3.2 Atomic and band structure of amorphous IZO | 55 |
| Fig. 3.3 Band structures of OSs | 56 |
| Fig. 3.4 Local geometry around metal and oxygen | 58 |
| Fig. 3.5 The comparison between TB and DFT results | 64 |
| Fig. 3.6 The overlap integral and mobility in ZnO | 66 |
| Fig. 3.7 The crystal and electronic structure of c-IGZO | 69 |
| Fig. 3.8 Calculated Hall mobility in c-IGZO | 73 |
| Fig. 3.9 The relaxation time for each scattering source | 75 |

| | |
|--|-----|
| Fig. 3.10 Atomic structures of hydrogen impurity | 78 |
| Fig. 3.11 Charge densities of anionic hydrogen | 79 |
| Fig. 3.12 Averaged formation energies of hydrogen impurity | 81 |
| Fig. 3.13 Schematic diagram for transition energy between anionic and cationic hydrogen | 83 |
| Fig. 4.1 The unitcells of crystalline OSs | 90 |
| Fig. 4.2 The amorphous structure of a-IGZO | 91 |
| Fig. 4.3 Difference of dielectric constants between calculation and experiments | 94 |
| Fig. 4.4 Quasiparticle band gaps of OSs | 96 |
| Fig. 4.5 GW_0 band gaps | 99 |
| Fig. 4.6 The quasiparticle electronic structure of a-IGZO | 102 |
| Fig. 4.7 Weight of metals at conduction bottom in a-IGZO | 105 |
| Fig. 4.8 Tauc plots in c- and a-IGZO | 107 |

1.1 Overview of oxide semiconductor (OS)

In recent years, a great deal of interests in oxide semiconductors (OSs) which are based on the post-transition-metal like Cd, In, Ga, Zn and Sn have been rapidly growing for the application to the thin-film transistors (TFTs) for state-of-art transparent electronic devices owing to their unique properties of transparency as well as controllable conductivity without external doping.[1-3] In particular, the OS-based TFT which is fabricated at room-temperature shows good performance with high carrier mobility, which enables the realization of flexible and large-area electronic devices.[4-6]

The development of OS-based TFTs has been begun in earnest since 2003 when Nomura et al. announced successful fabrication of the TFTs using the single crystalline $\text{InGaO}_3(\text{ZnO})_5$ (sc-IGZO5) active layer.[3] Prior to the appearance of the sc-IGZO5, there have been the attempts to develop TFT using OSs, but the performance of TFT was not promising because it was difficult to control the carrier concentration of the oxides such as ZnO and In_2O_3 especially below 10^{17} cm^{-3} . [7,8] In addition, many grain-boundaries in OSs film substantially suppress the carrier mobility by grain-boundary scattering. For example,

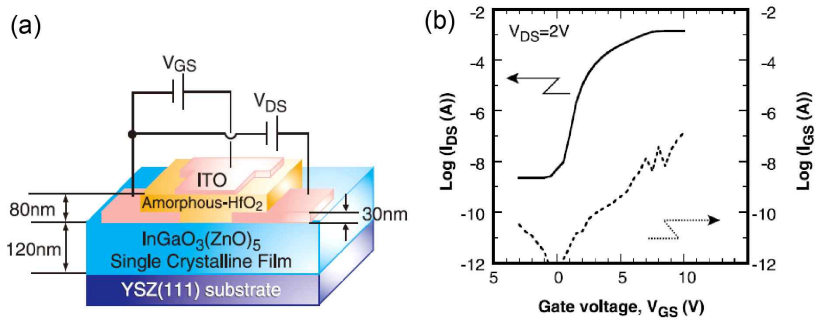


Figure 1.1. (a) Schematic TFT device structure using c-IGZO5 channel layer. (b) Transfer characteristics of sc-IGZO5 based TFT.[3]

it was reported that ZnO TFTs exhibited poor performance with $\sim 10^3$ on-off ratio showing normally-on characteristics or low field-effect mobility of $\sim 3 \text{ cm}^2/\text{Vs}$ due to many grain-boundaries in a normally-off device.[2,9,10] It was demonstrated that, however, the single crystalline phase of IGZO5 was stably deposited on the substrate and its TFT characteristics showed excellent performance with an on-off current ratio of $\sim 10^6$ and $\sim 80 \text{ cm}^2/\text{Vs}$ of field-effect mobility in the enhanced mode as shown in Fig. 1.[3]

More interestingly, TFT using amorphous In-Ga-Zn-O (a-IGZO) was developed in 2004.[4] The TFT with a-IGZO channel layer which was deposited on a plastic substrate showed excellent performances displaying the comparable electron mobility with that of its crystalline counterpart even though it was fabricated at room temperature without additional annealing process as shown in Fig 2.[4] Because it has been difficult to produce high-performance device using low-temperature fabrication method due to a trade-off relation between fabrication temperature and device performance, the appearance of a-IGZO has attracted tremendous interests triggering the intensive researches on OSs.

One of the promising applications of OSs is the large-area and flexible display.[11-14] That is because (i) the possibility of the low temperature fabrication of oxide semiconductor TFTs assures the uniformity of the device characteristics which is a key factor for large-area and flexible devices and (ii) the high carrier mobility of OSs leads to the fast switching of the image on the wide display. By

this time, the hydrogenated amorphous Si (a-Si:H) is actively utilized for the display application, but it suffers from the low carrier mobility below $\sim 1 \text{ cm}^2/\text{Vs}$. As the realization of next-generation display with ultra definition, large area, and three-dimensional effect requires the TFTs with the higher carrier mobility than $\sim 20 \text{ cm}^2/\text{Vs}$, [14,15] the OSs have attracted a great many of interests as an alternative to a-Si:H.

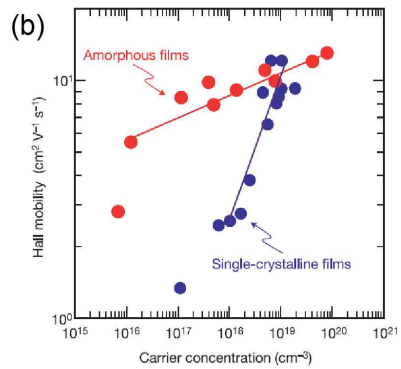
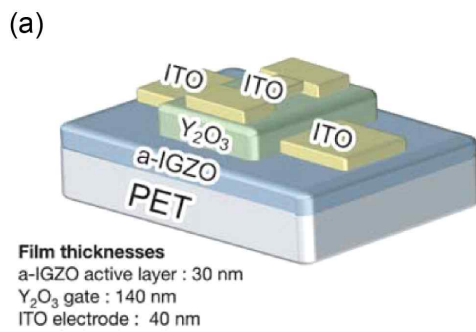


Figure 1.2. (a) Device structure of TFT. a-IGZO channel layer deposited on a plastic substrate. (b) Hall mobility of amorphous and crystalline IGZO films.[4]

1.2 Challenges in the utilization of OS

1.2.1 Transport mechanisms of electrons in OS

The electron mobility is a figure of merit for the TFT performance and the relatively high value of the mobility is strength of the OS in comparison with that of a-Si:H. However, further increment of the mobility is still demanded for the next-generation display application. As such, it is important to understand the fundamental electron behavior including the band structure and the scattering mechanisms.

In experiment, the abnormal transport characteristics of the electrons in OSs depending on carrier concentration and temperature are observed. For example, It was reported that the electron mobility of the binary OSs like ZnO and In_2O_3 was reduced with increasing carrier density up to $\sim 10^{19} \text{ cm}^{-3}$, but further doping enhanced the electron mobility as shown in Fig. 3, which is not observed in other semiconductors like Si and GaAs.[16-18]

One of the explanation for such upshift of the mobility at high carrier density is the grain-boundary scattering mechanism.[18,19] In this mechanism, the increase of carrier density leads to the abundance of the electrons with the high energy near Fermi level, which provides more opportunities for the electrons to propagate between grains with effectively lower energy barrier.

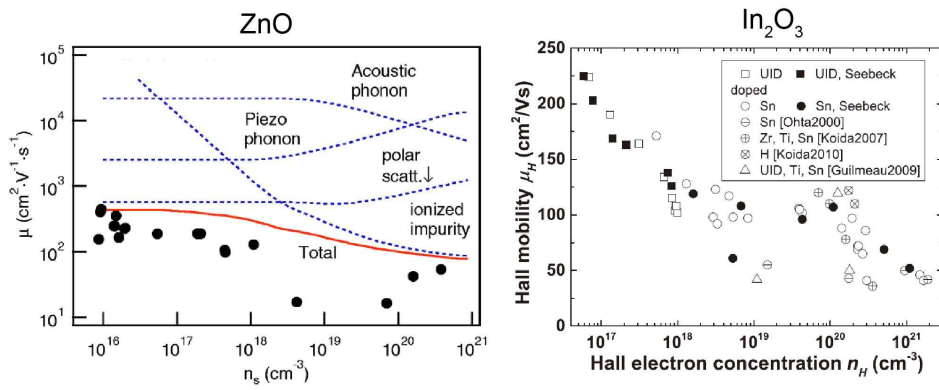


Figure 1.3. Electron mobility in ZnO (left)[16] and In_2O_3 (right)[17] as a function of carrier concentration. The upshifts of the electron mobility at $\sim 10^{19} \text{ cm}^{-3}$ of carrier concentration are shown in both cases.

The upshift of the mobility, however, is observed for the epitaxially grown single crystalline ZnO while other (poly)crystalline elemental or compound semiconductors rarely show such behavior.[16] Thus, the grain-boundary scattering is not sufficient to explain the mobility enhancement in OSs at high carrier density and the underlying mechanisms for that remained unclear.

Furthermore, in c- and a-IGZO, the prototypical multicomponent OS, it was observed that increasing carrier concentration or temperature enhances the carrier mobility.[20, 21] This enhancement of the carrier mobility is not found in typical semiconductor like Si where large carrier density or high temperature usually reduce the mobility due to further scattering process from the ionized impurity and the phonon, respectively.[22-24]

In order to figure out this unique transport behavior, two models were proposed. First, Kamiya et al. accounted for the electron transport in c- and a-IGZO by percolation model.[20] They focused on the disordered atomic structure in not only a-IGZO but also in c-IGZO where there are no preferential atomic sites between Ga and Zn. In percolation model, itinerant electrons propagate along the low-energy path in the random potential energy surface created by the atomic disorder. Meanwhile, Tomai et al. suggested a hopping model where the electrons hop among the spatially localized sites by gaining the thermal energy for overcoming the energy barrier among the sites.[25] Even though these two models explain carrier concentration and temperature dependence of the electron mobility in c- and a-IGZO, they are not

predictive model since they rely on the empirical parameters for reproducing the experimental data.

1.2.2 Degradation phenomena in OS device

While OSs are promising alternatives to a-Si:H for application to active layer of TFTs in display device, many researches have raised various instability problems of the oxide semiconductor TFT. Generally, the oxide semiconductors are transparent and most of photons within visible range are not absorbed due to large optical band gap, but it was reported that the visible and UV light illumination on the oxide semiconductor TFT creates a fair amount of the photocurrent and the photo-induced conducting state remains for hours or days, even in the absence of light as shown in Fig. 4(a). This long-lived photo-conducting state is called persistent photoconductivity (PPC) and it has been known as a critical drawback of oxide semiconductor TFT.[26-28]

In addition, experimentally, the threshold voltage (V_{TH}) shift of the oxide semiconductor TFT has been observed under gate bias stress conditions.[29-33] Specifically, Fig. 4(b) show that the application of the positive gate bias for turning on the TFT leads to a positive shift in the V_{TH} and the impact of the negative gate bias is vice versa as shown in Fig. 4(c). Besides, the illumination of visible and UV light accelerates the negative shift in V_{TH} under the negative gate bias condition and the transfer characteristics of the TFT is deteriorated increasing subthreshold swing as shown in Fig. 4(d).[34-36] More serious problem is that these V_{TH} shifts are not recover right after removing the gate bias stress and it takes hours or days for full recovery. As a

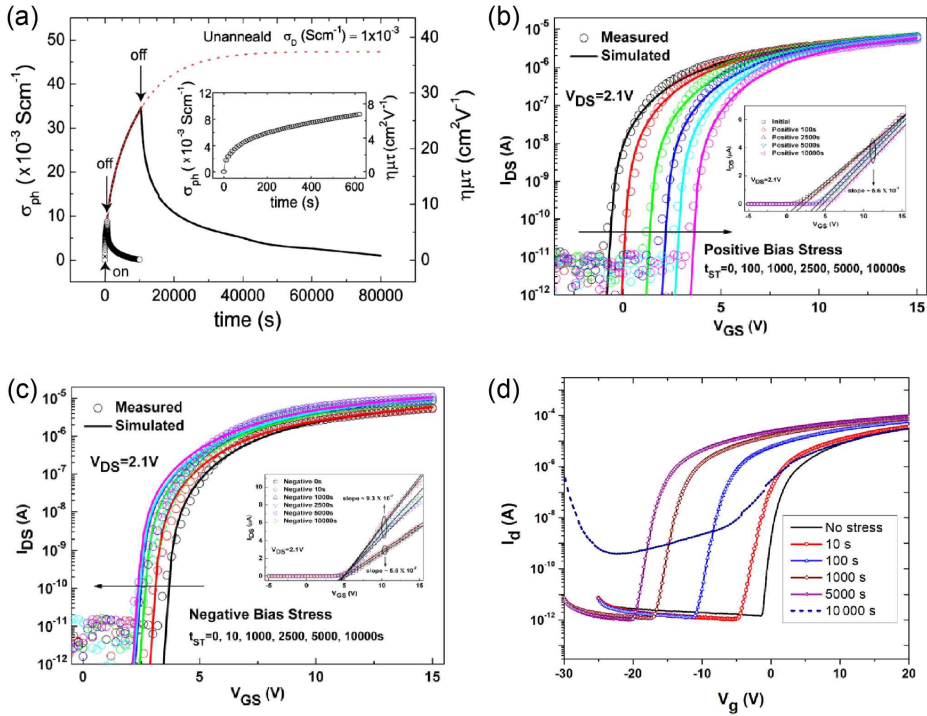


Figure 1.4. (a) Persistent photoconductivity in IGZO.[26] (b) and (c) show transfer characteristics with positive and negative shift of the threshold voltage under positive and negative bias stress, respectively.[29] (d) The variation of transfer curve under 410 nm light illumination with -20 V gate bias.[34]

result, this slow recovery of V_{th} shift is considered as a major hurdle to be solved for long-term stability of oxide semiconductor TFT.

1.3 Goal of the dissertation

The main purpose of this study is to reveal the microscopic origin for the optical and electrical properties of OSs using *ab-initio* calculation technique for developing OSs with high mobility as well as outstanding stability. The density functional theory (DFT) based quantum simulation method is used to understand the materials property. On the basis of the DFT calculation results, the analysis to understand the electrons behavior when a solid is exposed to the various stress conditions such as the light illumination and the electric field are performed.

Specifically, we focus on the abnormal electron transport characteristics in OSs. In contrast to well known semiconductors like Si and GaAs, the electron mobilities of OSs in amorphous phase are comparable with those in crystalline phase. In addition, the mobilities in crystalline In_2O_3 and ZnO show the minimum values at $\sim 10^{19} \text{ cm}^{-3}$ of carrier concentration and enhancement at higher carrier concentration, which are not theoretically understood clearly yet. To reveal the microscopic origin of such electronic transport characteristics, we employ generalized model Hamiltonian for the conduction band of OSs based on tight-binding approximation and obtain the eigenstate and the dispersion relation. The results show that the highly dispersive quasi-linear band structures arise in OSs due to the interaction between metal s and oxygen p orbitals regardless of the phase of OSs, which accounts for why the electron mobility in amorphous OSs is as high as that in crystalline OSs. Furthermore, the electron mobility in

ZnO is calculated on the basis of the quasi-linear conduction band by solving Boltzmann transport equation, it is found that the electron mobility is enhanced at $\sim 10^{19} \text{ cm}^{-3}$ of carrier concentration due to the reduction of the back scattering probability at high carrier concentration which is the nature of the quasi-linear band structure.[37]

On the other hand, the previous experimental results show that electron mobility increases within a wide range of carrier concentration ($10^{16} \sim 10^{20} \text{ cm}^{-3}$) and temperature (10 ~ 300 K). To address the enhancement of electron mobility, we develop the scattering model focusing on the cation disorder in c-IGZO in which Ga and Zn are randomly distributed at the symmetrically equivalent sites. The results show that the cation disorder plays a critical role as a dominant scattering center limiting the electron mobility in c-IGZO below 100 cm^2/Vs and it is the origin of enhancement of electron mobility at high carrier concentration and temperature.[38] Above studies related with electronic structure and transport mechanism of OSs will serve as the groundwork for developing new OSs with high electrons mobility.

Furthermore, we study the impact of the hydrogen defect in amorphous OSs which is easily introduced into OSs during the fabrication of the device. The material we study is the amorphous In-Sn-Zn-O (a-ITZO) and it exhibits the good TFT performance with high electron mobility and on/off ratio. We classify the hydrogen defect into four different types according to their charge states and atomic positions. The DFT calculations reveal that the charge state of the

hydrogen defect can be converted depending on Fermi levels, which contributes to the V_{TH} shifts under illumination and bias stress.[39] Through the result of this study, we can extend the understand of the effect of the defects on the performance of the electronic device utilizing OSs, which gives a guideline to better the stability of the TFT using OS under various stress conditions.

On the other hand, in spite of the large optical band gap of OSs, there are still non-negligible photo absorption of the light with visible range. Various origins for such sub-gap absorption like defect, grain-boundary, and disordered atomic structure are suggested, but microscopic understanding is still limited. In this study, many-body perturbation theory based on GW approximation is used for the correction of the DFT band gaps. We test GW calculations extensively for various binary OSs and optimize the calculation setups of GW calculation for correct band gaps.[40] Moreover, we applied GW calculation on a-IGZO to find the origin of the visible light absorption, as visible light absorption critically influences on the instability problems in a-IGZO. While the defect related with non-stoichiometry like oxygen vacancy can be possible origin for the sub-gap absorption, the tail states near the band edge in amorphous materials is also able to be intrinsic source for that kind of light absorption. Our results show the light absorption with the shorter wave length than blue which severely deteriorates the instability of the V_{TH} mainly originates from the long valence tail states and the downshift of the conduction band minimum due to the undercoordinated In atoms.[41] From this part, as

we reveal the relation between atomic structure and optical absorption of OSs, we can aid to develop the device using OSs which is robust to the illumination stress.

1.4 Organization of the dissertation

This dissertation includes six chapters. Chapter 1 is the introduction part of this study. In chapter 2, we account for the theoretical backgrounds and the basic concept that are employed in this study. In next three chapters, we discuss the electronic properties including the transport properties and the impacts of the hydrogen defect of OS (chapter 3) and the optical absorption in OS (chapter 4). Finally, we summarize the overall results of this study in chapter 5.

1.5 Bibliography

- [1] T. Kamiya et al., *NPG Asia Mater.* 2, 15 (2010).
- [2] R. L. Hoffman et al., *Appl. Phys. Lett.* 82, 733 (2003).
- [3] K. Nomura et al., *Science* 300, 1269 (2003).
- [4] K. Nomura et al., *Nature* 432, 488 (2004).
- [5] H. Yabuta et al., *Appl. Phys. Lett.* 89, 112123 (2006).
- [6] M. Kim et al., *Appl. Phys. Lett.* 90, 212114 (2007).
- [7] M. W. J. Prins et al., *Appl. Phys. Lett.* 68, 3650 (1996).
- [8] M. W. J. Prins et al., *Appl. Phys. Lett.* 70, 458 (1997).
- [9] P. F. Carcia et al., *Appl. Phys. Lett.* 82, 1117 (2003).
- [10] R. L. Hoffman et al., *J. Appl. Phys.* 95, 5813 (2004).
- [11] J. S. Park et al., *Thin Solid Films* 520, 1679 (2012).
- [12] J.-H. Lee et al., *Soc. Inf. Display Digest* 39, 625 (2008).
- [13] M.-C. Sung et al., *Proc. IMID2007*, 9-1 (2007).
- [14] H.-S. Kim et al., *Sci. Rep.* 3, 1459 (2013).
- [15] T. Kamiya et al., *Sci. Technol. Adv. Mater.* 11, 044305 (2010).
- [16] T. Makino et al., *Appl. Phys. Lett.* 87, 022101 (2005).
- [17] N. Preissler et al., *Phys. Rev. B* 88, 085305 (2013).
- [18] K. Ellemer et al., *Thin Solid Films* 516, 5829 (2008).
- [19] K. Ellmer et al., *J. Phys. D: Appl. Phys.* 34, 3097 (2001).
- [20] T. Kamiya et al., *J. Disp. Technol.* 5, 462 (2009).
- [21] K. Nomura et al., *Appl. Phys. Lett.* 85, 1993 (2004).
- [22] N. A. Poklonski et al., *J. Appl. Phys.* 93, 9749 (2003).

- [23] D. Chattopadhyay et al., *Rev. Mod. Phys.* 53, 745 (1981).
- [24] T. Dietl et al., *J. Phys. Chem. Solids* 39, 1041 (1978).
- [25] S. Tomai et al., *Jpn. J. Appl. Phys., Part 1* 51, 03CB01 (2012).
- [26] D. H. Lee et al., *Electrochem. Solid-State Lett.* 13, H324 (2010).
- [27] D. H. Lee et al., *Thin Solid Films* 518, 3000 (2010).
- [28] S. Jeon et al., *Nat. Mater.* 11, 301 (2012).
- [29] E. N. Cho et al., *IEEE Trans. Device Mater. Rel.* 11, 112 (2011).
- [30] J.-M. Lee et al., *Appl. Phys. Lett.* 93, 093504 (2008).
- [31] H.-S. Kim et al., *IEEE Electron Device Lett.* 32, 1251 (2011).
- [32] J. Raja et al., *Appl. Phys. Lett.* 102, 083505 (2013).
- [33] M. D. H. Chowdhury et al., *Appl. Phys. Lett.* 98, 153511 (2011).
- [34] R. N. P. Vemuri et al., *J. Phys. D: Appl. Phys.* 46, 045101 (2013).
- [35] H. Oh et al., *Appl. Phys. Lett.* 97, 183502 (2010).
- [36] T. -C. Chen et al., *Surf. Coat. Technol.* 231, 465 (2013).
- [37] Y. Kang et al., *Phys. Rev. Lett.* 108, 196404 (2012).
- [38] Y. Kang et al., *Appl. Phys. Lett.* 102, 152104 (2013).
- [39] Y. Kang et al., *Adv. Electron. Mater.* 2015, 1400006 (2015).
- [40] Y. Kang et al., *Phys. Rev. B* 89, 165130 (2014).
- [41] Y. Kang et al., *APL Materials* 2, 32108 (2014).

2.1. Density functional theory (DFT)

2.1.1 Hohenberg and Kohn theorem

All the macroscopic properties of matters are governed by the microscopic behavior of the electrons which is determined by the quantum mechanics. To predict quantum mechanical nature of the electrons, Schrödinger's equation should be solved. In a solid, there are periodic positive ions potentials as in a crystal lattice and electrons move around them. The Hamiltonian is then

$$\begin{aligned}
 H = & \sum_i^N -\frac{\hbar^2 \nabla_i^2}{2M_i^2} + \frac{1}{2} \sum_{i=1}^N \sum_{j \neq i}^N \frac{Z^2 e^2}{|\vec{R}_i - \vec{R}_j|} + \sum_k^N -\frac{\hbar^2 \nabla_k^2}{2m} \\
 & + \frac{1}{2} \sum_{k=1}^N \sum_{l \neq k}^N \frac{e^2}{|\vec{r}_k - \vec{r}_l|} - \sum_{i=1}^N \sum_{j=1}^N \frac{Ze^2}{|\vec{r}_k - \vec{R}_i|}. \quad (2.1)
 \end{aligned}$$

where (\vec{R}_i, \vec{R}_j) and (\vec{r}_k, \vec{r}_l) are positions of ions and electrons, respectively, Ze is the nuclear charge of ion, (M_i, m) are the mass of the nuclei and electron, respectively. In Eq. 2.1, First two terms are

the kinetic energy of ions (KE_{ion}) and the potential energy between ions (PE_{ion}), respectively. And third and fourth terms corresponds to the kinetic energy of electrons (KE_e) and the potential energy between electrons (PE_e), respectively. The last term represents the potential energy between electron and ion (PE_{ion-e}). Since the mass of a nucleus is much heavier than that of an electron, the characteristic velocity of a nucleus is much slower in comparison with that of an electron. Therefore, for describing electrons' motion, the first two terms in Eq. 2.1 can be ignored practically, and they are separately treated. This is the Born-Oppenheimer approximation and the Hamiltonian we should deal with is

$$H = \sum_k^N -\frac{\hbar^2 \nabla_k^2}{2m} + \frac{1}{2} \sum_{k=1}^N \sum_{l \neq k}^N \frac{e^2}{|\vec{r}_k - \vec{r}_l|} - \sum_{i=1}^N \sum_{j=1}^N \frac{Ze^2}{|\vec{r}_k - \vec{R}_i|}. \quad (2.2)$$

As a result, this Hamiltonian is starting point for investigating the influence of the electrons on the properties of a solid.

Schrödinger's equation considering the Hamiltonian in Eq. 2.2 is normally many-body problem except for hydrogen atom and there is no analytic solution for that. One of the approximate methods to solve above equation is the density functional theory (DFT). The DFT calculation has been considered as a powerful tool to predict the properties of matters with fair accuracy and reasonable computational cost. The key point of the DFT calculations is based on Hohenberg and

Kohn theorem.[1] Theorem 1 says that the ground state density, $n(\vec{r})$, is uniquely determined for an external potential, $v(\vec{r})$, applied to any interacting systems assuming that the ground state is not degenerate. In theorem 2, it is proved that a unique universal functional of the density, $F[n(\vec{r})]$, independent of the external potential exist as follows:

$$E = \int v(\vec{r})n(\vec{r})d\vec{r} + F[n(\vec{r})]. \quad (2.3)$$

2.1.2 Kohn-Sham equation

In 1965, Kohn-Sham introduced fictitious orbitals $(\phi_i(\vec{r}), i = 1, \dots, N)$ which give the charge density as follows:

$$n(\vec{r}) = \sum_{i=1}^N |\phi_i(\vec{r})|^2. \quad (2.4)$$

To find the ground state charge density and its energy, the variational principles is applied to total energy in Eq. 2.3 in terms of $\phi_i(\vec{r})$. Then the we can get one-particle equation for each orbital:

$$\left[-\frac{\hbar^2}{2m}\nabla^2 + v_{eff}(\vec{r})\right]\phi_i(\vec{r}) = \epsilon_i\phi_i(\vec{r}). \quad (2.5)$$

This equation is called Kohn-Sham equation.[2] As a result, $\phi_i(\vec{r})$ becomes a non-interacting fermion which moves under the effective potential, $v_{eff}(\vec{r})$, which is given by:

$$v_{eff}(\vec{r}) = v_{ion-e}(\vec{r}) + v_{e-e}(\vec{r}) + v_{xc}(\vec{r}). \quad (2.6)$$

where $v_{ion-e}(\vec{r})$, $v_{e-e}(\vec{r})$, and $v_{xc}(\vec{r})$ are the ionic potential of nucleus, the electron-electron Coulomb potential which is only dependent upon

charge density (Hartree potential), and the exchange-correlation potential. The $v_{xc}(\vec{r})$ is responsible for many-body interaction between electrons and its exact form in terms of the charge density is not known. Therefore, the various approximations for that have been introduced and we discuss it in chapter 2.2.

On the other hand, it is noted that the Eq. 2.5 is well defined when the charge density which is the solution we want find is known. Thus, the Eq. 2.5 is solved by self-consistent method as shown in Fig. 2.1. To be specific, we put an initial guess of the charge density as a solution into the Eq. 2.1 and determine the new charge density. When old and new charge density is quite different over the certain criteria, next guess is build by mixing old and new ones. If the difference between input and output charge densities is below the given criteria, then the iteration is finished.

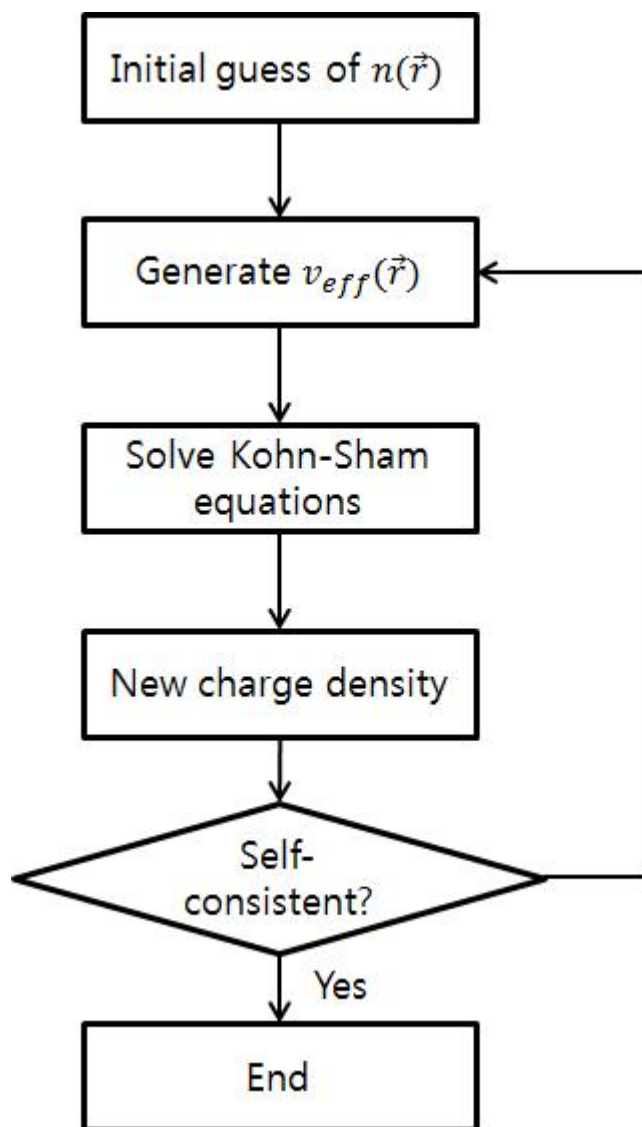


Figure 2.1. Schematic figure for the self-consistent iteration to solve Kohn-Sham equations.

2.2 Exchange–correlation energy

2.2.1 Local density approximation (LDA)

As a first approximation, we consider the interacting homogeneous electron gas for which the form of exchange–correlation energy can be known precisely. Since the total energy for the homogeneous system can be expressed in a perturbation expansion in terms of the charge density, the $v_{xc}(\vec{r})$ in a form of density functional can be obtained. If we assume that the exchange–correlation energy of a many–electron system relies on the local density identically with homogeneous electron gas, it is called local density approximation (LDA).[2] The exchange–correlation energy in LDA, $E_{xc}^{LDA}(\vec{r})$, is given by:

$$E_{xc}^{LDA} = \int v_{xc}^{LDA}[n(\vec{r})]n(\vec{r})d\vec{r}. \quad (2.7)$$

The LDA is good approximation for metallic systems in which the electrons behave like homogeneous electron gas. However, the LDA inherently fails to predict the electronic structure for insulators because the behavior of electrons is deviated from the homogeneous system. The representative error is the self-interaction of electrons. In Hartree potential, the Coulomb potential is only dependent upon charge density which includes the spurious self-repulsion interaction. This

self-interaction error must be disappeared, but in LDA, this error is still remained. Therefore, the LDA calculation tends to delocalize the electrons, which causes critical problems for localized electrons in d- and f-orbitals.

On the other hand, it was reported that the exact exchange-correlation energy has derivative discontinuity at the integer number of electrons. However, the LDA results in convex form of energy variation with respect to the number of electrons as shown in Fig. 2.2, which gives rise to the underestimation of the band gap of insulator.[3]

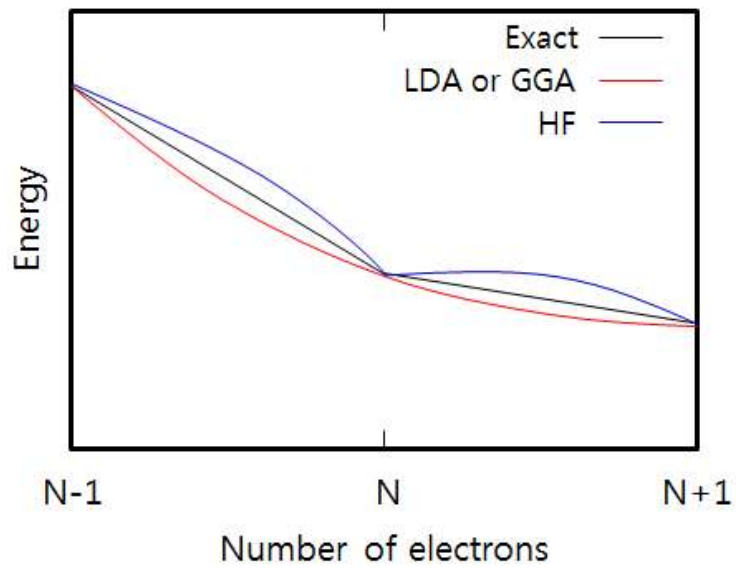


Figure 2.2. Schematic diagram for the energy change depending on exchange-correlation functional with respect to the number of electrons.

2.2.2 Generalized gradient approximation (GGA)

To reflect the influence of the inhomogeneity of the electron density on exchange–correlation energy, the semiempirical generalized gradient approximation (GGA) appeared. In addition to the local density information, the GGA functional uses information of local density gradient and its exchange–correlation energy is given by:

$$E_{xc}^{GGA} = \int v_{xc}^{GGA}[n(\vec{r}), |\nabla n(\vec{r})|]n(\vec{r})d\vec{r}. \quad (2.8)$$

There are various distinct GGA functional depending on the formalism related with the density gradient dependent exchange–correlation energy. One of the widely used GGA functionals is PW91 which was proposed by Perdew and Wang in 1992.[4] One of the challenges for developing the GGA functional is to satisfy the sum rule for the exchange–correlation holes and the PW91 achieved that by introducing the cutoff density. Because the PW91 was the first reliable GGA functional, there were several problems, Perdew, Burke, and Ernzerhof newly developed Perdew–Burke–Ernzerhof (PBE) functional which improved own problems in the PW91.[5]

The GGA functionals like PW91 and PBE typically (but not always) give more accurate results than the LDA. For example, the GGA shows better results for the binding energy of the molecules or the cohesive energy than the LDA. However, the GGA still undergoes the

self-interaction error and the lack of derivative discontinuity in the GGA is also still found as shown in Fig. 2.2.

2.3 Beyond the DFT

2.3.1 DFT+U

The main idea of the DFT+ U method is to separate electrons into localized and delocalized electrons and the on-site Coulomb interaction energy for the localized electrons like d and f orbitals is taken into account by Hubbard like term as follows:

$$E^{DFT+U} = E^{DFT} + \frac{U}{2} \sum_{i \neq j} n_i n_j - \frac{UN(N-1)}{2}, \quad (2.9)$$

where U is the on-site Coulomb interaction, n_i is the occupancy of d and f orbitals. The second term in Eq. 2.9 represents the electron–electron Coulomb energy of d and f orbitals and last term is the double counting part which should be removed due to the energy contribution in the DFT functional. The U is defined by:

$$U = [E(d^{n+1}) + E(d^{n-1})] - 2E(d^n). \quad (2.10)$$

where d^n is the number of electrons in d (or f) orbitals. This definition shows the U is the average energy change for adding and removal of an electron in localized orbitals.

In this approach, we can get the orbital eigenvalues by taking the

derivative of the total energy with respect to the occupancy of that orbital according to Janak's theorem:

$$\epsilon_i = \frac{\partial E_{DFT+U}}{\partial n_i} = \epsilon_i^{DFT} + U\left(\frac{1}{2} - n_i\right). \quad (2.11)$$

Equation 2.1 shows that the eigenvalue of the occupied orbital is down shifted by $U/2$ making the electron localized on particular orbital and if the state is unoccupied, its eigenvalue increases by $U/2$.

2. 3. 2 Hybrid functional

In chemical point of view, there is a well known approximation for the many-body effect, which is called Hartree-Fock (HF) approximation. This approximation is appropriate for the localized system and it could be thought as the opposite limit in contrast to the DFT based on the homogeneous electron system. If we take a single Slater determinant of the occupied one-electron states as the total wavefunction (this is because electrons are fermion), it gives non-local Fock exchange energy as follows:

$$E_x^{HF} = -\frac{e^2}{2} \sum_{i,j} \int \int \frac{\phi_i^*(\vec{r})\phi_j^*(\vec{r}')\phi_i(\vec{r}')\phi_j(\vec{r})}{|\vec{r}-\vec{r}'|} d\vec{r}d\vec{r}'. \quad (2.12)$$

In HF approximation, the self-interaction energy in Hartree term is completely canceled by Fock exchange energy. This method is quite good approximation for the finite system like a molecule and according to Koopman's theorem, the ionization potential (IP) of the system which is required energy for removing an electron from the system corresponds to its highest occupied molecular orbital (HOMO) levels in HF calculation. However, it misses the correlation effect between electrons, which can lead to large error in comparison with experimental results.

Neglect of the correlation energy in HF approximation tend to

exaggerate the localization of the electrons on the specific orbital showing the concave form of the energy change with respect to the occupation of the state as shown in Fig. 2.2.

Recently, a hybrid functional method which admixes the DFT and HF exchange–correlation energy is proposed in a spirit of complement between the DFT and the HF method. Depending on the ratio for mixing the energies, there are various kinds of hybrid functional methods like B3LYP[6] and PBE0[7]. Even though these hybrid functionals improve the results of the DFT and the HF, the time cost for calculation of the non-local Fock exchange energy over the whole space was quite burden. Therefore, Heyd-Scuseria-Ernzerhof suggested the way to separate the bare Coulomb potential into short-range (SR) and long-range (LR) parts:

$$\frac{1}{r} = SR_{\mu}(r) + LR_{\mu}(r) = \frac{erfc(\mu r)}{r} + \frac{erf(\mu r)}{r}, \quad (2.13)$$

where erf and $erfc$ are error function and complementary error function, respectively, and μ is the parameter to define the range-separation.[8] Then, the Fock exchange energy is only calculated for the SR part. This separation can be justified by the fact that the bare Coulomb potential is screened by the electrons in solid state, which effectively reduces the long-range contribution in the exchange energy.

As a results, the exchange–correlation energy of the hybrid functional

in a manner of Heyd-Scuseria-Ernzerhof (HSE) is given by:

$$E_{xc}^{HSE} = \alpha E_x^{SR}(\mu) + (1 - \alpha) E_x^{PBE,SR}(\mu) + E_x^{PBE,LR}(\mu) + E_c^{PBE}. \quad (2.14)$$

Typical values of α and μ are 0.25 and 0.2 \AA^{-1} (HSE06),[9] respectively, and HSE06 functional have been yielded good results like band gaps and lattice parameters for most of solid systems as shown in Fig. 2.3.

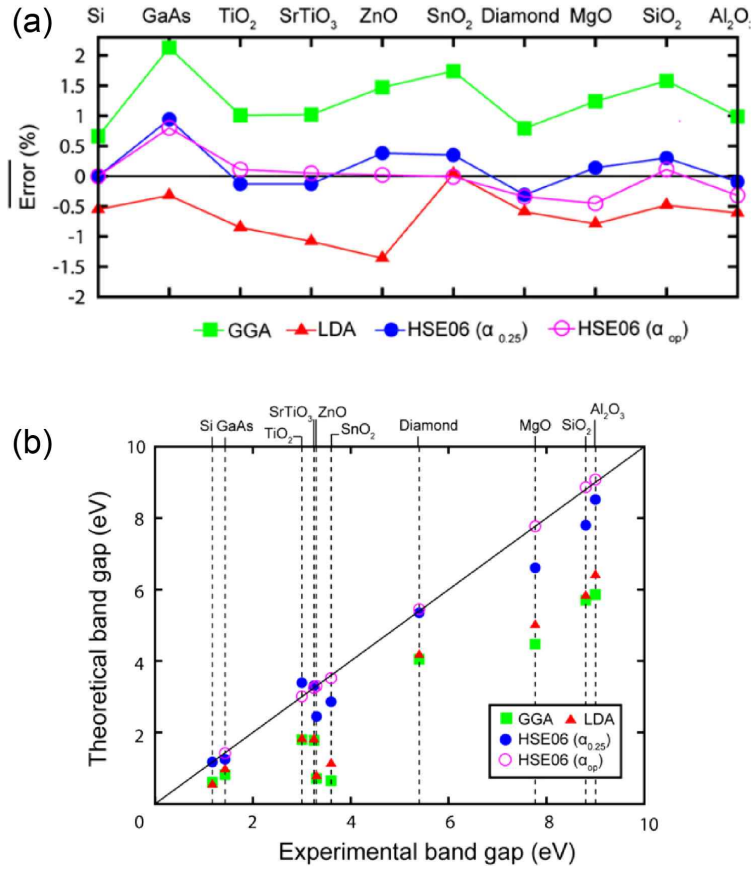


Figure 2.3. (a) The lattice parameters and (b) the band gap of LDA, GGA, and HSE hybrid functionals.[10]

2.3.3 GW approximation

The lack of derivative discontinuity in the conventional DFT functionals like LDA and GGA causes the band gap underestimation of the insulators. The fundamental physical origin for that is the neglect of the many-body effect in their exchange-correlation energy. Recently, incorporation of such many effects has been achieved by using the many-body perturbation theory based on GW approximation. The GW approximation deals with the quasiparticle which consists of an electron and screening charge cloud and the quasiparticle energy levels of the GW calculation correspond to the (inverse)photoemission experimental results.

Present implementation of the GW calculation usually utilizes the DFT wavefunction and eigenvalues as inputs and the quasiparticle levels ($\epsilon_{n\vec{k}}$) and wavefunction ($\phi_{n\vec{k}}$) are determined perturbatively as follows[11]:

$$\epsilon_{n\vec{k}} = Re[\langle \phi_{n\vec{k}} | T + V_{ion} + V_H + \Sigma(\epsilon_{n\vec{k}}) | \phi_{n\vec{k}} \rangle], \quad (2.15)$$

where T is the kinetic energy operator, V_{ion} is the ionic potential, V_H is the Hartree potential, and Σ is the self-energy operator. The Eq. 2.15 is updated by the linearization method on the basis of the Newton-Raphson scheme. In the GW approximation, the Σ is given by:

$$\Sigma(\vec{r}, \vec{r}', \epsilon) = \frac{i}{4\pi} \int e^{i\omega'\delta} G(\vec{r}, \vec{r}', \epsilon + \omega') W(\vec{r}, \vec{r}', \omega') d\omega' \quad (2.16)$$

where G and W are the Green's function and the screened Coulomb interaction, respectively, and δ is an infinitesimal. The Green's function is given by:

$$G(\vec{r}, \vec{r}', \epsilon) = \sum_{nk} \frac{\phi_{nk}(\vec{r}) \phi_{nk}^*(\vec{r}')}{\epsilon - \epsilon_{nk} \mp i\delta}, \quad (2.17)$$

and the screened Coulomb interaction is evaluated by:

$$W(\vec{r}, \vec{r}', \epsilon) = \int \epsilon^{-1}(\vec{r}, \vec{r}'', \epsilon) v(\vec{r}'', \vec{r}) d\vec{r}'', \quad (2.17)$$

where v is the bare Coulomb operator and ϵ is the dielectric function which can be evaluated in random phase approximation (RPA). Usually, the quantum calculation package using the periodic boundary condition, the self-energy is evaluated in the reciprocal space.

There are several levels of the self-consistency for calculating self-energy depending on whether ϕ_{nk} and ϵ_{nk} are updated or not during the iteration. In the one-shot G0W0 calculation, the quasiparticle energy is evaluated by using ϕ_{nk} and ϵ_{nk} of the DFT calculation without further iteration. If we impose the self-consistency in G only

or both of G and W with respect to $\epsilon_{n\vec{k}}$, they are called GW0 and GW schemes, respectively. And $\phi_{n\vec{k}}$ together with $\epsilon_{n\vec{k}}$ can be updated in G only or both of G and W , which are called QPGW0 and QPGW, respectively.

2.4 Electron transport

2.4.1 Fermi-Golden rule

The electrons in a solid with periodic potential are described by Bloch waves and those in different quantum states are completely orthogonal. If there is no perturbation to break the periodicity of the potential, the scattering event from one state to another state is not occur. However, the imperfection like point defects or phonon can leads to the electrons scattering which is one of the most important phenomenon in determining of the electron transport properties.

To determine the scattering probability (or scattering rate), the time-dependent Schodinger' s equation in the below should be solved[12].

$$[H_0 + H']\Psi(\vec{r},t) = i\hbar \frac{\partial \Psi(\vec{r},t)}{\partial t}, \quad (2.18)$$

where H_0 and H' are the time-independent Hamiltonian operator for the unperturbed system and additional scattering potential, respectively, and $\Psi(\vec{r},t)$ represents a wavefunction. The solution of the Eq. 2.18 can be expressed by linear combination of the wavefunctions of the unperturbed system. If we assume that the H' is sufficiently small in comparison with the H_0 , we can approximately solve the Eq. 2.18 and

the final scattering rate, $S_{k, \vec{k}}$, between \vec{k} th state to \vec{k}' th state is given by:

$$S_{k, \vec{k}} = \frac{2\pi}{\hbar} \left| H_{k', \vec{k}}^a \right|^2 \delta(E(\vec{k}') - E(\vec{k}) - \hbar\omega) + \frac{2\pi}{\hbar} \left| H_{k', \vec{k}}^e \right|^2 \delta(E(\vec{k}') - E(\vec{k}) + \hbar\omega), \quad (2.19)$$

where $H_{k', \vec{k}}^{a(e)}$ is the matrix element of the scattering potential between \vec{k} and \vec{k}' state for absorption(emission) process with energy of $\hbar\omega$ and δ is the Kronecker delta function. This result is known as Fermi's Golden Rule.

The matrix element is defined by:

$$H_{k', \vec{k}} \equiv \int \phi_{k'}^*(\vec{r}) H \phi_{\vec{k}}(\vec{r}) d\vec{r}. \quad (2.20)$$

For the Bloch state, it can be evaluated approximately as follows:

$$H_{k', \vec{k}} \simeq \frac{1}{V} \int e^{-i\vec{k}' \cdot \vec{r}} H e^{i\vec{k} \cdot \vec{r}} d\vec{r} \int_{\Omega_{cell}} \mu_{k'}^*(\vec{r}) \mu_{\vec{k}}(\vec{r}) d\vec{r} = H(\vec{k}' - \vec{k}) I_{k', \vec{k}}, \quad (2.21)$$

where $\mu_{\vec{k}}$ is the periodic part of the Bloch wavefunction of \vec{k} state. As a result, the matrix element is separated into two parts; one is the Fourier transformation of the scattering potential, $H(\vec{k}' - \vec{k})$, and the other is the overlap integral between periodic parts of the Bloch

wavefunctions in \vec{k} and \vec{k}' states, $F_{\vec{k}',\vec{k}}$. In the case of the free electron, the $F_{\vec{k}',\vec{k}}$ is given by one, but fundamentally it depends on the character of the wavefunctions of \vec{k} and \vec{k}' states.

2.4.2 Boltzmann transport equation

For calculating the electron mobility, we need to know the particle distribution, $f(\vec{r}, \vec{v}, t)$, within a hyperspace of momentum and position. The classical equation for describing the time evolution of $f(\vec{r}, \vec{v}, t)$ is the Boltzmann transport equation and if we consider a electron which is expressed by the Bloch wavefunction with momentum quantum number, \vec{k} , the equation can be shown as semi-classical form as follows:[12]

$$\frac{\partial f(\vec{r}, \vec{k}, t)}{\partial t} = -\frac{1}{\hbar} \nabla_{\vec{k}} E(\vec{k}) \cdot \nabla_{\vec{r}} f - \frac{F}{\hbar} \cdot \nabla_{\vec{k}} f + \left(\frac{\partial f}{\partial t} \right)_S + \left(\frac{\partial f}{\partial t} \right)_{G-R}, \quad (2.22)$$

where E and F are the energy of electrons and electric field, respectively, S is the scattering, G is the generation, and R is the recombination. First two terms on the right side in the Eq. 2.22 are the streaming part and the last two terms are for the distribution change due to the scattering and the electron generation and recombination.

The analytic solution for the Eq. 2.22 can be obtained under relaxation time approximation and low electric field. If we assume that the electrons exhibit uniform distribution, it is in steady-state, and there is no generation and recombination, then the Eq. 2.2 becomes

$$\frac{F}{\hbar} \cdot \nabla_{\vec{k}} f = \left(\frac{\partial f}{\partial t} \right)_S = -\frac{f_a}{\tau_r}, \quad (2.23)$$

where the f_a is the anti-symmetric part of the electron distribution under the non-equilibrium situation and τ_r is the relaxation time. By solving the Eq. 2.23, we can get the electron distribution under the bias, which enable us to calculate the mean drift velocity of the electrons along the field direction. Finally, the electron drift mobility, μ_n , is determined by the relationship between mean drift velocity and the electric field,

$$\mu_n = \frac{q \langle \langle \tau_r \rangle \rangle}{m^*}, \quad (2.24)$$

where q and m^* are the electron charge and the effective mass. The $\langle \langle \tau_r \rangle \rangle$ is the mean relaxation time considering energy dependence of the τ_r .

2.5 Optical absorption in insulator

The dielectric function is the complex quantity;

$$\varepsilon(\hat{q}, \omega) = \varepsilon_1(\hat{q}, \omega) + i\varepsilon_2(\hat{q}, \omega), \quad (2.25)$$

where ε_1 and ε_2 are the real and imaginary parts, respectively. \hat{q} and ω stand for the wave vector and the frequency of the incident light, respectively. The ε_1 and ε_2 are related with the optical absorption and the dielectric screening, respectively. The frequency dependent dielectric function can be evaluated within the DFT formalism. If we neglect the local field effect, the macroscopic dielectric constant is given by

$$\varepsilon_2(\hat{q}, \omega) = \frac{4\pi^2 e^2}{\Omega} \lim_{q \rightarrow 0} \frac{1}{q^2} \sum_{c,v,k} 2w_k \delta(\epsilon_{c\vec{k}+\vec{q}} - \epsilon_{v\vec{k}} - \omega) \times \left| \langle \mu_{c\vec{k}+\vec{q}} | \mu_{v\vec{k}} \rangle \right|^2, \quad (2.26)$$

where c and v represents the conduction and the valence band states, respectively, w_k is the k-point weight, Ω is the unitcell volume, and ϵ and μ are the energy and the periodic part of the wavefunctions of the Bloch waves, respectively.[13] The real part of the dielectric function can be obtained by the Kramers-Kronig transformation

$$\varepsilon_1(\hat{q}, \omega) = 1 + \frac{2}{\pi} P \int_0^\infty \frac{\varepsilon_2(\hat{q}, \omega') \omega'}{\omega'^2 - \omega^2} d\omega', \quad (2.27)$$

where P denotes the principal value. The optical absorption coefficient (α) for the light with the photon energy of E_{ph} is given by

$$\alpha(E_{ph}) = \frac{\sqrt{2} E_{ph}}{\hbar} \left[\sqrt{\varepsilon_1^2(E_{ph}) + \varepsilon_2^2(E_{ph})} - \varepsilon_1(E_{ph}) \right]^{1/2}. \quad (2.27)$$

2.6 Defect formation energy

The defect formation energy (E^f) of a defect with charge q (D^q) within the supercell formalism is evaluated by:

$$E^f(D^q) = E_{tot}^{D^q} - E_{tot}^{bulk} + \mu_D + q(E_v + E_F), \quad (2.24)$$

where $E_{tot}^{D^q}$ is the total energy of the supercell with a D^q , E_{tot}^{bulk} is the total energy of the supercell without a defect, μ_D is the chemical potential of the defect, E_v is the valence band maximum, and E_F is the Fermi level. The μ_D is the variable that reflects the experimental growing condition.[14,15]

The E^f is the thermodynamic quantity which indicates the required energy for creating a defect in a material. Thus, the defect with the relatively low E^f can be more existed than others. Since a defect can be charged by donating or accepting the electrons from the E_F , the E^f depends on the E_F . The meaningful values of the E_F is located between band gap of the semiconductors and the stable charge configuration of the defect can be changed depending on the E_F . The E_F position which shows the formation energies of charge state q and q' are same is called transition level, $\epsilon(q/q')$, and it can be evaluated by

$$\epsilon(q/q') = \frac{E^f(D^q; E_F = 0) - E^f(D^{q'}; E_F = 0)}{q' - q}. \quad (2.25)$$

2.7 Bibliography

- [1] P. Hohenberg et al., Phys. Rev. 136, B864 (1964).
- [2] W. Kohn et al., Phys. Rev. 140, A1133 (1965).
- [3] P. Mori-Sanchez et al., Phys. Rev. Lett. 100, 146401 (2008).
- [4] J. P. Perdew et al., Phys. Rev. B 45, 13244 (1992).
- [5] J. P. Perdew et al., Phys. Rev. Lett. 77, 3865 (1996).
- [6] A. D. Becke et al., J. Chem. Phys. 98, 5648 (1993).
- [7] M. Ernzerhof et al., J. Chem. Phys. 110, 5029 (1999).
- [8] J. Heyd et al., J. Chem. Phys. 118, 8207 (2003).
- [9] A. V. Krukau et al., J. Chem. Phys. 125, 224106 (2006).
- [10] S. Park et al., Curr. Appl. Phys. 11, S337 (2011).
- [11] M. Shishkin et al., Phys. Rev. B 75, 235102 (2007).
- [12] B. K. Ridley et al., *Quantum Process in Semiconductors* (Oxford University Press, New York, 1993). 3rd ed.
- [13] M. Gajdos et al., Phys. Rev. B 73, 45112 (2006).
- [14] Y. Kumagai et al., Phys. Rev. B 89, 195205 (2014).
- [15] S. Lany et al., Phys. Rev. Lett. 98, 2007 (2007).

3.1. Introduction

In this chapter, we deal with electronic properties of OSs especially in terms of carrier mobility and defect which should be investigated for improving the performance of the TFT.[1-3] First, we are going to discuss two important aspects of the electron transport characteristics in the OS. One is about the universal quasi-linear band structure which plays an important role for determining the electron mobility in the highly doped OS. The other one is as to the scattering mechanisms in the crystalline In-Ga-Zn-O where the electron mobility is quite low even in the single crystalline phase in comparison with single crystalline semiconductors and the increase of the temperature and the carrier density enhance the electron mobility. In addition, we will discuss influence of the hydrogen defect on the device degradation of the OS-based TFT because the ubiquitous hydrogen in the atmosphere is a defect which can be easily introduced into OSs during the deposition process.[4,5] We investigate the behavior of the hydrogen impurity in amorphous In-Zn-Sn-O (a-IZTO) using the DFT calculation.

3.2. Calculation method

The analytic dispersion relation of the universal conduction band of OSs are obtained by the tight-binding (TB) model. The model Hamiltonian is set on the basis of the orthonormal basis set which is similar with atomic orbitals of $|s\rangle$, $|w\rangle$, and $|p\rangle$ corresponding to metal s , and oxygen s and p orbitals, respectively. The existence of these virtual orbital basis set can be confirmed by the maximally localized Wannier functions (MLWFs) [6] and the examples for ZnO in the zinc blende structure are shown in Fig. 3.1. It is noted that the MLWFs in ZnO well reproduce the shape of the metal s , and oxygen s and p orbitals (but not completely same).

The band structures of OSs are obtained by using the DFT calculations using the Vienna *ab-initio* simulation package (VASP).[7] The energy cutoff of 500 eV for the plane-wave basis set is used for all materials and \vec{k} -point is sampled to ensure the energy convergence within 10 meV/atom. The atomic structures are relaxed until the atomic forces are reduced below 0.02 eV/Å. The GGA+ U functional is employed for the exchange-correlation energy and the effective U values for In $4d$, Zn $3d$, Sn $4d$ are 7, 7.5, and 3.5 eV, respectively.

The amorphous structures of OSs were generated by melt-quenching simulation. First, they were melted at 2500 K and rapidly quenched to the 0 K with the -50 K/ps quenching rate. The final structure was further optimized at 0 K calculation.

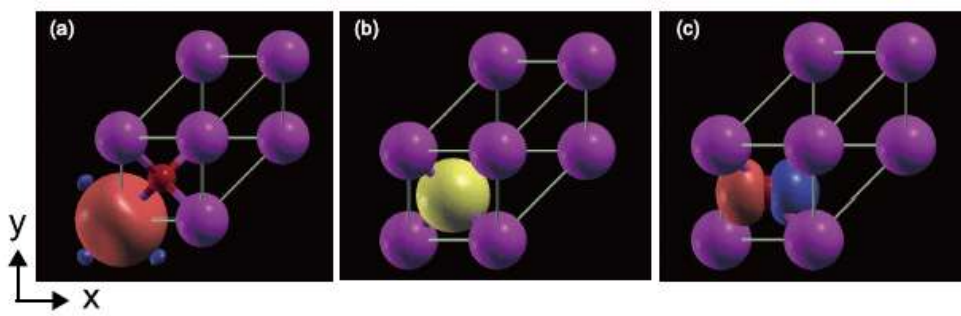


Figure 3.1. MLWFs in the zincblende ZnO. The purple and red sphere represent Zn and O atoms.[8]

The DFT calculation for a-IZTO is performed using PBE exchange–correlation energy. To generate amorphous atomic structure, first, we randomly distribute the atoms in a cubic supercell with the constraints on the bond lengths between atoms. 10 formula units of $\text{In}_2\text{SnZn}_2\text{O}_7$ were included within a supercell and it was heated at 3000 K for 10 ps and rapidly cooled down to 300 K at a quenching rate of -300 K/ps.

The final amorphous structure was fully relaxed at 0 K until every force acting on all the atoms is converged below 0.02 eV/Å using GGA+ U functional. The U values for semicore d electrons of In, Zn, and Sn are 5.0, 7.5, and 3.5 eV, respectively. The kinetic energy cutoff for plane-wave basis set was 500 eV and single k-point of (0.25, 0.25, 0.25) was used for the k-point sampling.

3.3. Result and discussion

3.3.1 Quasi-linear band structure in OS

It was reported that the electron mobility of the amorphous OS is comparable with that of the crystalline counterpart[9] and this is partially supported by the DFT calculations which universally show the similar conduction band in both of the crystalline and amorphous phase.[10-12] However, it has not been understood how such large dispersion can be shown in the amorphous material. (This is not an artifact of the supercell approach with periodic boundary condition and to identify the existence of the dispersive conduction band, we confirmed that the conduction bands of the supercells with different lattice parameters along a specific direction are well maintained. This indicates the robust conduction band in the amorphous phase is not an artifact, but intrinsic property as shown in Fig. 3.2.)

In addition, the dispersion relations of the conduction bands of OSs commonly are associated with the that of the massive Dirac particle[13] in the form of $E = \sqrt{\epsilon^2 + \gamma^2 k^2}$ as shown in Fig. 3.3. All the conduction bands in Fig. 3.3 have the minimum point at Γ point and displays the isotropic dispersion regardless of their compositions or atomic structures as shown in insets in Fig. 3.3 which show the Fermi surface at Fermi level at the carrier density of $10^{20}\sim 10^{21}$ cm⁻³ at 0 K. Even though, the fact that the conduction bands in OSs are insensitive to the atomic

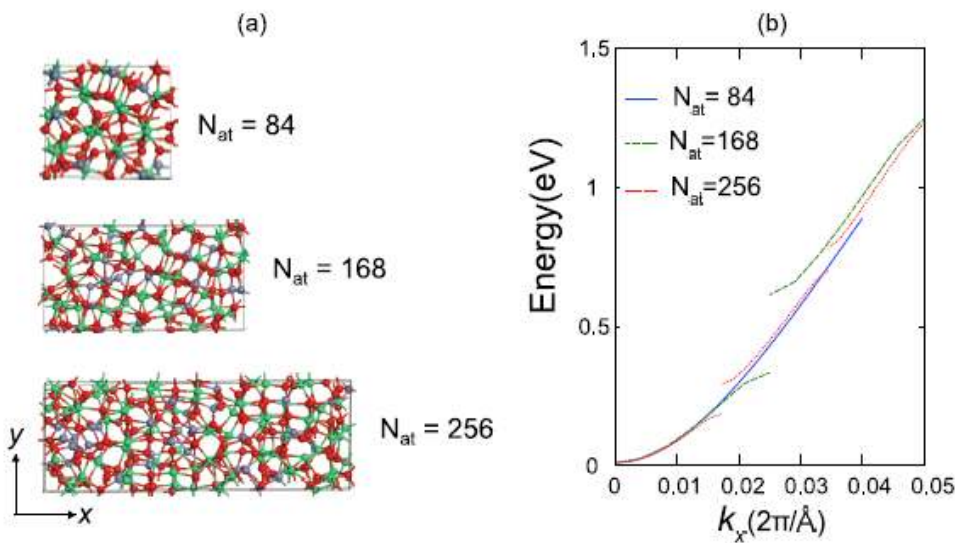


Figure 3.2. (a) amorphous InZnO (a-IZO) with different lattice constants. (b) The conduction bands of a-IZOs in (a). The conduction bands for larger supercell are unfolded and conduction bottom sets to '0'. [8]

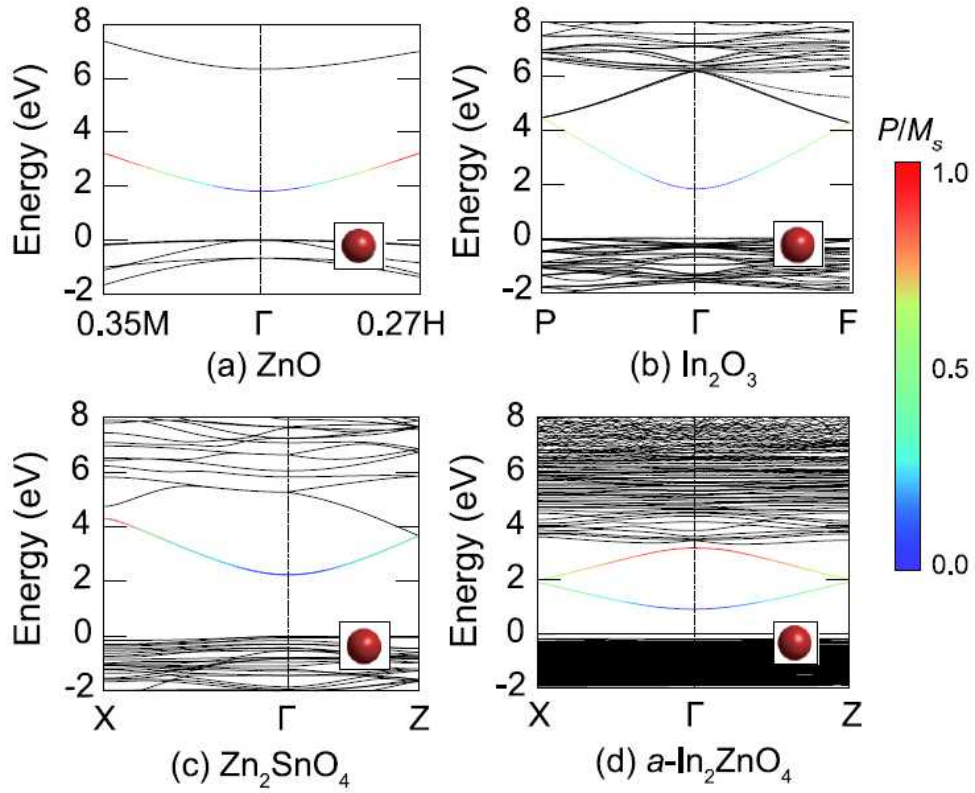


Figure 3.3. Band structure of (a) ZnO, (b) In_2O_3 , (c) Zn_2SnO_4 in inverse-spinel structure, and (d) In_2ZnO_4 in amorphous phase. The color indicates the ratio of weight of oxygen p orbitals (P) to that of metal s orbitals (M_s). The red spheres in insets represent Fermi surfaces at the carrier density of 10^{21} (crystal) and 10^{20} (amorphous) cm^{-3} . [8]

disorder can be partially supported by the overlap among the highly isotropic metal s orbital which is the main character of the conduction bottom, the contribution of the oxygen p orbital is not negligible as shown in Fig. 3.3. Therefore, we develop new microscopic theory to explain origin of the robust band structures in OSs by taking into account not only metal s but also oxygen s and p orbitals.

To obtain the Hamiltonian (H) matrix element, we examined the local atomic configurations around metal and oxygen in the crystalline and amorphous phase of OSs including In, Ga, Cd, Zn, and Sn atoms. It is found that the local configuration of the metals shows the tetrahedral or octahedral geometries except for Sn which has planar triangular coordinated by the oxygen atoms and all the oxygens exhibit tetrahedral geometry as shown in Fig. 3.4.[14]

In the lowest order of \vec{k} which is the Bloch vector, the matrix elements for the metal at the center of the oxygens in the tetrahedra or octahedra is given by

$$\left\langle s \left| H \sum_j^N e^{i\vec{k} \cdot \vec{d}_j} \right| p_{\hat{n},j} \right\rangle \simeq -i\gamma^s \vec{k} \cdot \hat{n}, \quad (3.1)$$

where N is the number of the nearest neighboring oxygen atoms, \vec{k} is the Bloch vector, \vec{d}_j is the displacement vector from the metal to the j th neighboring oxygen atoms, and $|p_{\hat{n},j}\rangle$ is the j th oxygen p orbitals indicating the \hat{n} direction. The γ^s is the hopping integral between metal s and oxygen p orbitals. This relation will be denoted by “paralle

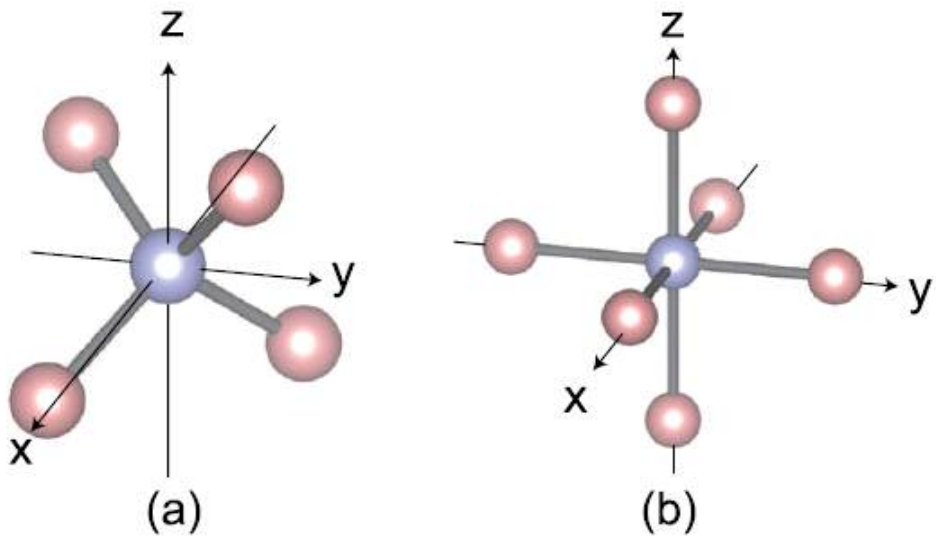


Figure. 3.4. Schematic diagrams of the local atomic configuration around metal and oxygen atoms in OSs. (a) Tetrahedral and (b) octahedral geometries. [8]

coupling” .[8] The corresponding mathematical formular between $|s\rangle$ and $|w\rangle$ is

$$\left\langle s \left| H \sum_j^N e^{i\vec{k} \cdot \vec{d}_j} \right| w_j \right\rangle \simeq \alpha^s, \quad (3.2)$$

where α^s is the hopping term for the metal s and oxygen s orbitals. The relation in the Eq. 3.2 will be called “isotropic coupling” . We assume that the hopping term between metal s orbitals beyond first nearest neighbor is constant (β) due to the large coordination number.

If we assume that the neighboring metals are same, the similar relation in the case of the oxygen at the center of the metal tetrahedron can be hold in the following way:[3]

$$\left\langle p_{\hat{n}} \left| H \sum_j^N e^{i\vec{k} \cdot \vec{d}_j} \right| s_j \right\rangle \simeq i\gamma^p \vec{k} \cdot \hat{n}, \quad (3.3)$$

$$\left\langle w \left| H \sum_j^N e^{i\vec{k} \cdot \vec{d}_j} \right| s_j \right\rangle \simeq \alpha^w, \quad (3.4)$$

where j runs over the nearest neighboring metal atoms. The hopping term from the oxygen to atoms beyond the second nearest neighbor is neglected due to the spatially localized nature of the oxygen p orbitals.

The construction of the Bloch-like state ($|\Psi_{\vec{k}}\rangle$) can be achieved by the linear combination of whole $|s\rangle$, $|w\rangle$, and $|p\rangle$ as follows:

$$|\Psi_{\vec{k}}\rangle = c_1 |S_{\vec{k}}\rangle + c_2 |W_{\vec{k}}\rangle + c_3 |P_{x,\vec{k}}\rangle + c_4 |P_{y,\vec{k}}\rangle + c_5 |P_{z,\vec{k}}\rangle, \quad (3.5)$$

where $\{c_i\}$ is the coefficient, $|S_{\vec{k}}\rangle = \sqrt{1/q} \sum_{j=1}^q e^{i\vec{k} \cdot \vec{d}_j} |s_j\rangle$,

$|W_{\vec{k}}\rangle = \sqrt{1/r} \sum_{j=1}^r e^{i\vec{k} \cdot \vec{d}_j} |w_j\rangle$, and $|P_{\hat{n},\vec{k}}\rangle = \sqrt{1/r} \sum_{j=1}^r e^{i\vec{k} \cdot \vec{d}_j} |p_{\hat{n},j}\rangle$. The q and r are the number of the metals and oxygens in the whole system. This

linear combination of the orbitals leads to the 5×5 Hamiltonian matrix for the binary oxides:

$$H = \begin{pmatrix} \epsilon^s + \beta & \alpha & -i\gamma k_x & -i\gamma k_y & -i\gamma k_z \\ \alpha & \epsilon^w & 0 & 0 & 0 \\ i\gamma k_x & 0 & \epsilon^p & 0 & 0 \\ i\gamma k_y & 0 & 0 & \epsilon^p & 0 \\ i\gamma k_z & 0 & 0 & 0 & \epsilon^p \end{pmatrix}, \quad (3.6)$$

where $\epsilon^{s,w,p}$ represent the on-site energy of $|S_{\vec{k}}\rangle$, $|W_{\vec{k}}\rangle$, and $|P_{\hat{n},\vec{k}}\rangle$. $\alpha = \sqrt{q/r} \alpha^s = \sqrt{r/q} \alpha^w$, and $\gamma = \sqrt{q/r} \gamma^s = \sqrt{r/q} \gamma^w$. In addition, this Hamiltonian can be further reduced to the 4×4 matrix by building the anti-bonding state ($|\Sigma_{\vec{k}}\rangle$) between $|S_{\vec{k}}\rangle$ and $|W_{\vec{k}}\rangle$ in the form of $|\Sigma_{\vec{k}}\rangle = \cos\phi |S_{\vec{k}}\rangle - \sin\phi |W_{\vec{k}}\rangle$ ($0 < \phi < \pi/2$). The $\cos\phi$ and $\sin\phi$ are the relative contributions of each basis, respectively. As a result, the Hamiltonian matrix is given by

$$H = \begin{pmatrix} \epsilon & -i\tilde{\gamma}k_x & -i\tilde{\gamma}k_x & -i\tilde{\gamma}k_x \\ i\tilde{\gamma}k_x & -\epsilon & 0 & 0 \\ i\tilde{\gamma}k_y & 0 & -\epsilon & 0 \\ i\tilde{\gamma}k_z & 0 & 0 & -\epsilon \end{pmatrix}, \quad (3.7)$$

where $\tilde{\gamma} = \gamma \cos \phi$ the on-site energies in the diagonal components are shifted for the simplicity. The important property of this Hamiltonian is that it does not rely on the orientation of the oxygen and metal polyhedra implying that the discussion is still valid for the disordered system with orientational disorder like amorphous phase. In addition, this Hamiltonian can be extended to the multicomponent system with different metal types owing to the small difference of the hopping parameters among In-O, Zn-O, and Sn-O.

Through the diagonalization of this Hamiltonian, we can obtain the eigenstate and eigenvalue. The triply-degenerated states with lower eigenvalues are for the valence band which is not interest in this study. The remaining state is for the conduction band and its eigenstate and eigenvalue are given as follows:

$$E = \sqrt{\epsilon^2 + \tilde{\gamma}^2 k^2}, \quad (3.8)$$

$$|\Psi_{\vec{k}}\rangle = \sqrt{\frac{\lambda_1}{\lambda_1 + \lambda_2}} |\Sigma_{\vec{k}}\rangle + i \sqrt{\frac{\lambda_2}{\lambda_1 + \lambda_2}} |P_{\hat{k}, \vec{k}}\rangle, \quad (3.9)$$

where $\lambda_1 = \sqrt{\epsilon^2 + \tilde{\gamma}^2 k^2} + \epsilon$ and $\lambda_2 = \sqrt{\epsilon^2 + \tilde{\gamma}^2 k^2} - \epsilon$. The dispersion relation

of the conduction band corresponds to that of the massive Dirac particles as mentioned earlier and it exhibits quasi-linear form which approximately shows linear dispersion at the high energy region. In addition, the conduction band is highly isotropic with respect to the direction of \vec{k} only depending on its size. The important feature of the eigenstate in the Eq. 3.9 is that the oxygen p orbitals parallel to the \vec{k} only contributes, which results from the parallel coupling between metal s and oxygen p orbitals for the given local geometries.

To examine the validity of the TB results, we compare them with the DFT calculation results. Figure 3.5 (a) shows that the shape of the conduction bands of the DFT and TB of the zinc blende ZnO are well matched each other regardless of the direction of the \vec{k} . In addition, as expected in the TB calculation, the local projection to the orthogonal component of the oxygen p orbitals with respect to the \vec{k} is negligible in the DFT calculation as shown in Fig. 3.5 (b) (see $|P_{\perp}/M_s|$). On the other hand, the Fig. 3.5 (b) shows the contribution of the parallel part of the oxygen p orbitals relative to the metal s orbitals of the TB eigenstate (see $|P_{\parallel}/M_s|$) agrees well with the DFT calculation. In particular, we can explicitly observe the parallel coupling of the oxygen p orbitals in the charge density distribution of the DFT calculation in the Fig. 3.5 (c) and (d).

As mentioned in the foregoing discussion, the isotropic and parallel coupling conditions approximately hold for the amorphous phase, which means the quasi-linear band with \vec{k} is valid for the amorphous OSs in

spite of the lack of periodicity of the atomic arrangement. This is distinctive nature of OSs in comparison with other semiconductors like Si and GaAs. This is because the interactions between p orbitals in Si and GaAs cannot be neglected and the matrix elements between p orbitals in disordered phase are severely fluctuated site-to-site.[15,16] As a result, the wavefunction in such materials is spatially localized showing the flat band structure.

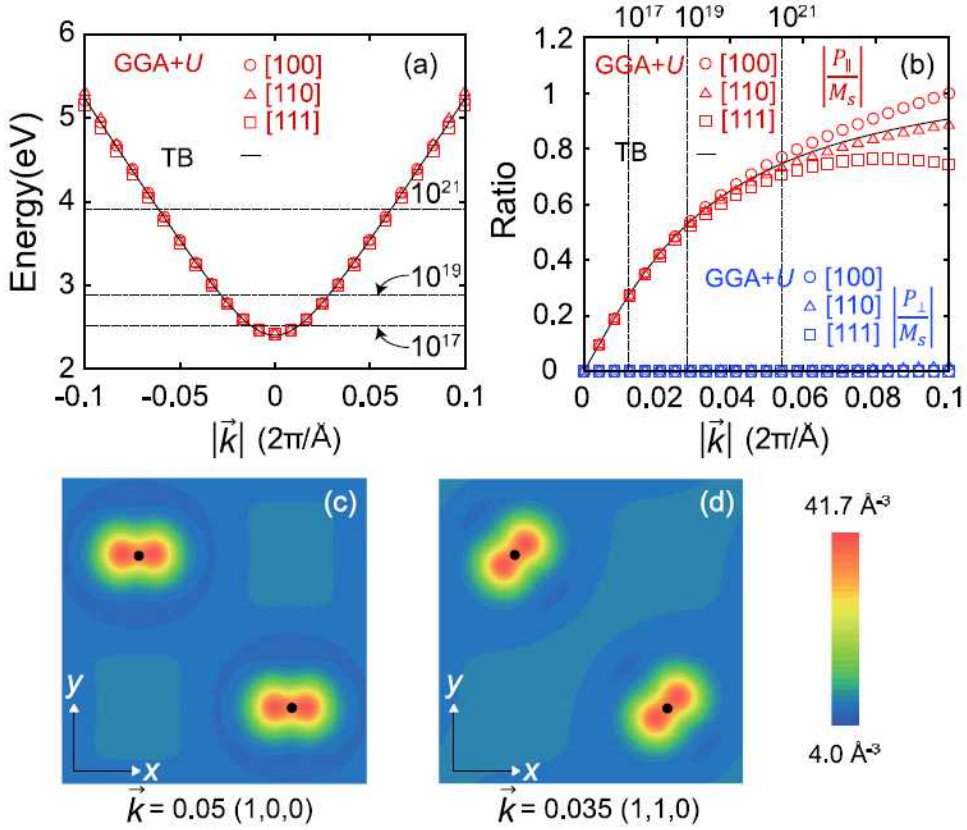


Figure 3.5. (a) Conduction bands of zinc blende ZnO along three different \vec{k} directions. The solid line is the fitted results of TB. The Fermi levels are presented for the 0 K carrier density of 10^{17} , 10^{18} , and 10^{19} cm $^{-3}$. (b) The relative contributions of oxygen p orbitals parallel or perpendicular to \vec{k} ($|P_{\parallel}/M_s|$ and $|P_{\perp}/M_s|$, respectively). The solid line represents the fitted data using TB. (c) and (d) display the charge density at specific \vec{k} points and the black dots are the oxygen atoms.[8]

3.3.2 Electron mobility in crystalline ZnO

The electron mobility of a semiconductor is one of the important factors to determine the performance of the electronic device. Usually, the electron mobility in semiconductors depends on the doping density and the temperature and increase of the doping density and the temperature drops the carrier mobility due to increase of the scattering.[17,18] In contrast to the well known semiconductors like Si and GaAs which showing the typical dependence of the carrier mobility as mentioned above, when the ZnO is doped, the abnormal upshift of the electron mobility at 10^{19} cm^{-3} was reported.[19] This is not understood in a simple free electron model.

In this study, the electron mobility in the ZnO is evaluated by applying the quasi-linear band structure. Several scattering mechanisms for determining the mobility can be considered and we performed the test calculation for the electron mobility taking into account the representative four scattering mechanisms. Among them, we selected two dominant scattering mechanisms, polar optical phonon (POP) and ionized impurity (II).

The relaxation time of each scattering mechanism is calculated by Fermi-Golden rule in the Eq. 2.19. The overlap integral part is explicitly evaluated by considering the eigenstate in the Eq. 3.9 instead of applying simple free electron model in which the overlap integral is typically set to 1.[20] Figure 3.6(a) shows the dependence of the

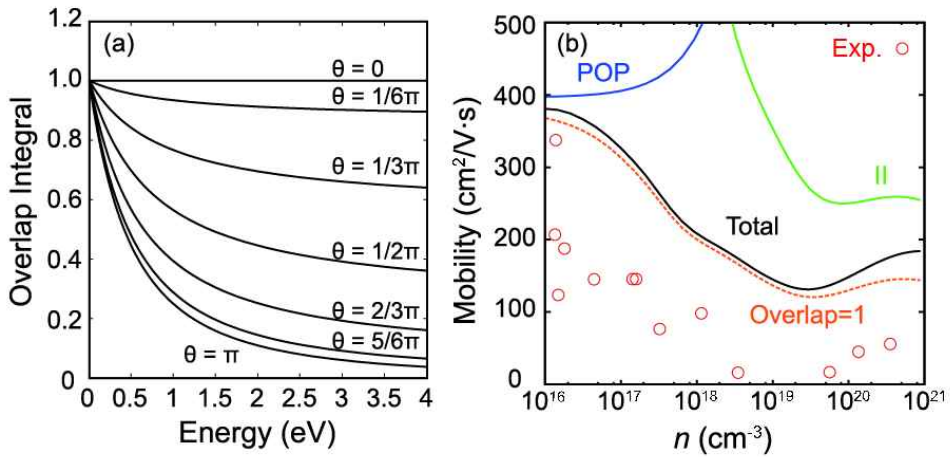


Figure 3.6. (a) The overlap integral of the lattice periodic parts of the eigenstates with respect to the scattering angle and electron energy. (b) The calculated total mobility of electrons in ZnO as a function of carrier densities.[8] The orange circles are experimental data in Ref. [19].

overlap integral for the II scattering on the electron energy and the scattering angle. It is noted that the overlap integral is highly reduced for the high angle scattering implying that the high angle scattering of electrons with high energy should be suppressed. This is the property of the eigenstate with linear-band structure and the similar behavior was also reported for the graphene which exhibits linear dispersion relation near the Fermi level.[21]

The total electron mobility is evaluated by Mathiessen's rule, $1/\tau_{tot} = 1/\tau_{POP} + 1/\tau_{II}$. Figure 3.6(b) displays the total calculated mobility together with those of each scattering mechanism. The POP scattering mainly determines the mobility in the low doping region and beyond 10^{18} cm^{-3} , the II scattering becomes dominant. The interesting point is that the total electron mobility is upshifted at $\sim 10^{19} \text{ cm}^{-3}$ and this feature is more enhanced than that of the overlap part set to one. Even though our calculation results is $\sim 100 \text{ cm}^2/\text{Vs}$ bigger than the experimental values due to the absence of the multiple scattering,[22] it well reproduces the experiments as shown in Fig. 3.6(b).

3.3.3 Electron mobility in crystalline In-Ga-Zn-O (IGZO)

The In-Ga-Zn-O (IGZO) is the most important OS in the application to the TFT. It provides good on/off ratio and high mobility regardless of the quality of their crystallinity.[23,24] The one of the remaining barriers for the realization of the device using IGZO is the further enhancement of the mobility.[25] Therefore it is important to understand the underlying transport mechanisms in IGZO.

It was reported that the electron mobility in crystalline IGZO (c-IGZO) increases with the temperature and the carrier density.[26,27] To explain such transport behavior, we focus on the unique structural feature in c-IGZO in which Ga and Zn are randomly distributed on the same crystallographic sites.[27] In other words, there is intrinsic atomic disorder in the c-IGZO.

Figure 3.7(a) shows the crystal structure of InGaZnO_4 (c-IGZO1) which is the representative composition of IGZO and the atomic positions of Ga and Zn exhibit the random distribution. Since the atomic disorder can make the electronic state localized because of the potential fluctuation, we checked the electronic structure for the c-IGZO1. The density of state near the Fermi level is shown in Fig. 3.7(b) with inverse participation ratio (IPR) which is the quantity estimating the degree of the localization of the given state. IPR is equal to $1/N$ when the state is distributed uniformly over N atoms and if the state is localized on just one atom, IPR is given by 1. As shown in Fig. 3.7(b),

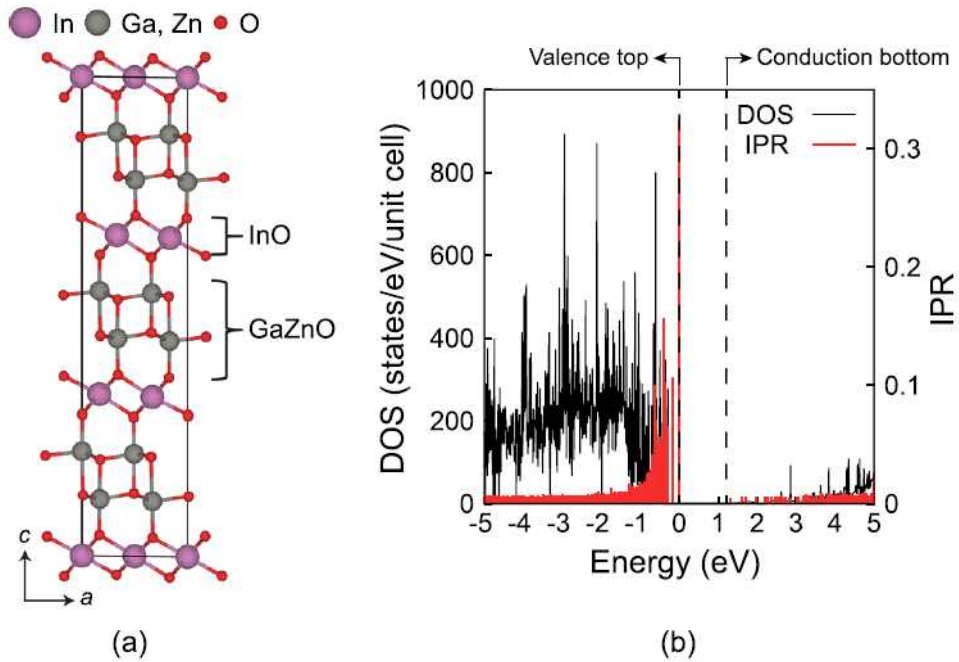


Figure. 3.7. (a) Crystal structure of IGZO1. The InO and GaZnO layers are alternatively piled along the c-axis. Ga and Zn are randomly distributed in GaZnO layers. (b) DOS and IPR of the IGZO1 supercell with 336 atoms.[28]

the states near the valence band maximum are highly localized due to the directionality of the oxygen p orbitals which are the main character of the valence band. In contrast to the valence band, the states near the conduction band minimum exhibit delocalized nature, which is explained by the universal Hamiltonian in Eq. 3.6. Therefore, we assume that the conduction electrons behave like the free electrons rather than the localized electrons.

The determination of the scattering mechanism in c-IGZO begins with the decomposition of the whole ionic potential $\{U(\vec{r})\}$ into a sum of effective potentials contributed by each atom;

$$U(\vec{r}) = \sum_{\text{In}} U_{\text{In}}(\vec{r} - \vec{R}_{\text{In}}) + \sum_{\text{Ga}} U_{\text{Ga}}(\vec{r} - \vec{R}_{\text{Ga}}) + \sum_{\text{Zn}} U_{\text{Zn}}(\vec{r} - \vec{R}_{\text{Zn}}) + \sum_{\text{O}} U_{\text{O}}(\vec{r} - \vec{R}_{\text{O}}), \quad (3.10)$$

where \vec{R}_{α} is the position of atom α . The $U(\vec{r})$ is separated into two parts; one is the aperiodic part due to the random distribution of Ga and Zn, $U_{\text{rand}}(\vec{r})$, and the other is the periodic part with the averaged virtual-crystal potential, $U_{\text{vc}}(\vec{r})$.

$$U_{\text{vc}}(\vec{r}) = \sum_{\text{In}} U_{\text{In}}(\vec{r} - \vec{R}_{\text{In}}) + \sum_{\text{O}} U_{\text{O}}(\vec{r} - \vec{R}_{\text{O}}) + \sum_{\text{Ga/Zn}} \left[f_{\text{Ga}} U_{\text{Ga}}(\vec{r} - \vec{R}_{\text{Ga/Zn}}) + f_{\text{Zn}} U_{\text{Zn}}(\vec{r} - \vec{R}_{\text{Ga/Zn}}) \right], \quad (3.11)$$

$$U_{rand}(\vec{r}) = \sum_{Ga/Zn} C_{Ga/Zn} \Delta U(\vec{r} - \overrightarrow{R_{Ga/Zn}}), \quad (3.12)$$

$$\Delta U(\vec{r}) = U_{Ga}(\vec{r}) - U_{Zn}(\vec{r}), \quad (3.13)$$

where $\overrightarrow{R_{Ga/Zn}}$ is the metal sites in GaZnO layers and $f_{Ga(Zn)}$ indicates the atomic ratio of the number of Ga(Zn) atoms to the total number of Ga and Zn atoms. $C_{Ga/Zn}$ in Eq. 3.12 represents a random function depending on the metal type at $\overrightarrow{R_{Ga/Zn}}$

$$C_{Ga/Zn} = \begin{cases} f_{Zn}, & \text{for } \overrightarrow{R_{Ga/Zn}} = \overrightarrow{R_{Ga}} \\ -f_{Ga}, & \text{for } \overrightarrow{R_{Ga/Zn}} = \overrightarrow{R_{Zn}} \end{cases}. \quad (3.14)$$

On the basis of the valence difference between Ga^{3+} and Zn^{2+} , it is assumed that the potential difference $\{\Delta U(\vec{r})\}$ in Eq. 3.13 is given by the screened Coulomb potential;

$$\Delta U(r) = -\frac{\Delta Z_{eff} q^2}{4\pi\epsilon_s r} e^{-r/L_s}, \quad (3.15)$$

where ΔZ_{eff} is the effective charge difference and ϵ_s and L_s are the static dielectric constant and screening length, respectively. As a result, we consider the Bloch-system with periodic potential of U_{vc} and the electron scattering arises from the U_{rand} .

The scattering rate from momentum \vec{k} to \vec{k}' is determined by the Fermi-Golden rule;

$$S_{\vec{k},\vec{k}'} = \frac{2\pi\Delta Z_{eff}^2 q^4 \rho_{Ga/Zn} f_{Ga} f_{Zn}}{V\hbar\epsilon_s^2 (|\vec{k}' - \vec{k}|^2 + 1/L_s^2)^2} \frac{2m_e^*}{\hbar^2} \delta(\vec{k}'^2 - \vec{k}^2), \quad (3.16)$$

where $\rho_{Ga/Zn}$ and V indicate the density of Ga/Zn sites and the volume of the system, respectively, and we call this cation disorder (CD) scattering rate.

The Hall mobility (μ_{Hall}) is obtained from the low-field solution of the Boltzmann transport equation considering the Hall factor $\langle\tau^2\rangle/\langle\tau\rangle^2$. [29] The $\langle\tau\rangle$ is the mean relaxation time and it can be independently determined for the ionized impurity (II), polar optical phonon (POP), CD scattering mechanisms. The total Hall mobility is obtained by applying the Mathiessen's rule to II, POP, and CD mobility. The materials parameters used in the mobility calculations are $\epsilon_\infty = 3.99$ (optical dielectric constant), $\epsilon_s = 9.06$, $m_e^*/m_e = 0.25$, and $\hbar\omega_{op} = 69.70$ meV (optical phonon energy). All the materials parameters for evaluating the Hall mobility are obtained by the DFT calculation except for ΔZ_{eff} which is considered as a parameter to give the best agreement with the experimental value. We assign 0.3 to ΔZ_{eff} , which is partially supported by the Bader charge analysis that results in 0.4 of ΔZ_{eff} . [30]

Figure 3.8(a) shows the Hall mobility of each scattering mechanism in the c-IGZO1 as a function of the temperature. For the temperature

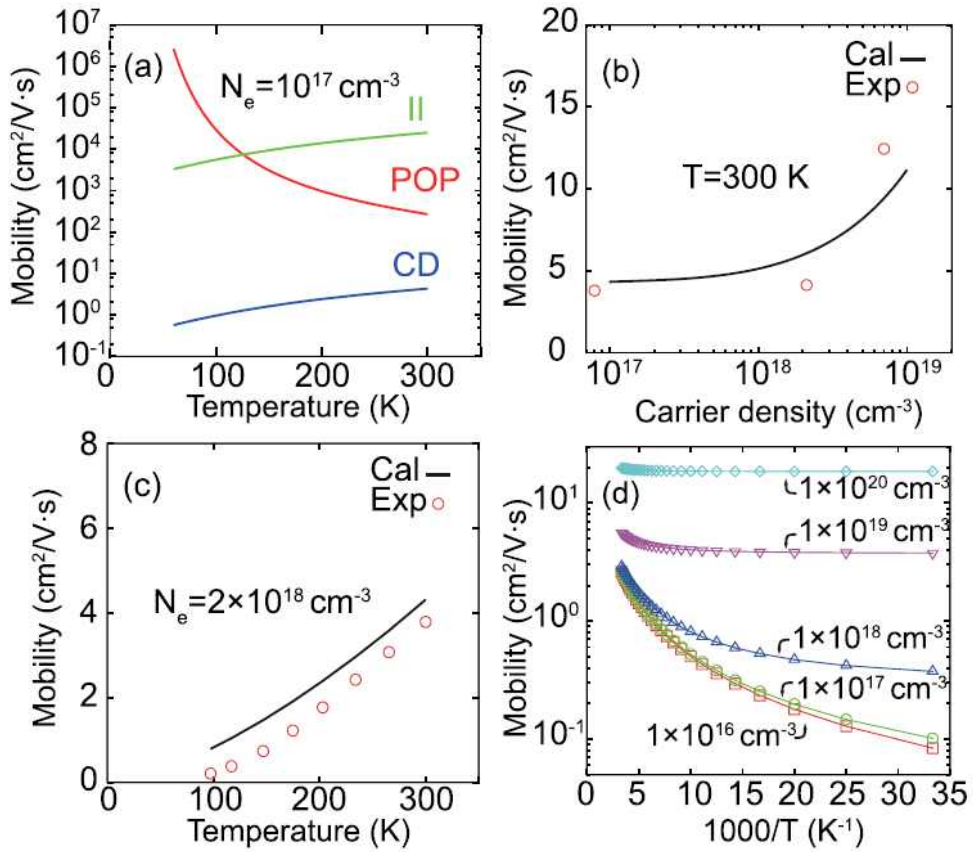


Figure 3.8. (a) Calculated Hall mobility for each scattering mechanism. (b)-(c) Theoretical Hall mobility and experimental data with respect to (b) carrier density and (c) temperature. (d) Temperature dependence of Hall mobility for various carrier concentrations.[28]

range from 0 K to 300 K, it is found that the CD scattering is the dominant scattering mechanism in comparison with other ones. The calculated Hall mobility for c-IGZO1 is compared with experimental results as shown in Fig. 3.8(b) and (c) and it is noteworthy that the theoretical mobility well describes the temperature and carrier concentration dependence of the Hall mobility in experiments.[26] In addition, our results show quantitatively good agreement with the experimental data implying that the CD scattering is the most important scattering mechanism in the c-IGZO. On the other hand, previous experimental research reported that the temperature dependence of the mobility in c-IGZO is reduced for the highly doped sample showing the metallic feature. Such transport behavior in experiments can be also observed as shown in Fig. 3.8(d). [26]

For explaining the temperature and carrier density dependence of the Hall mobility, we analysis the energy dependent relaxation time for each scattering mechanism and the electron distribution for different carrier density. The relaxation time of the CD scattering as shown in Fig. 3.8(a) exhibits increases with electron energy. As a result, the Hall mobility increases with the temperature and the carrier density. In addition, the thermally activated electrons at high carrier density (in this case, $N_e = 10^{20} \text{ cm}^{-3}$) occupy the states near ~ 0.3 eV above the conduction band minimum which gives the more slow change of the relaxation time of the CD scattering. Therefore, the Hall mobility of the samples with high carrier density is less sensitive to the temperature.

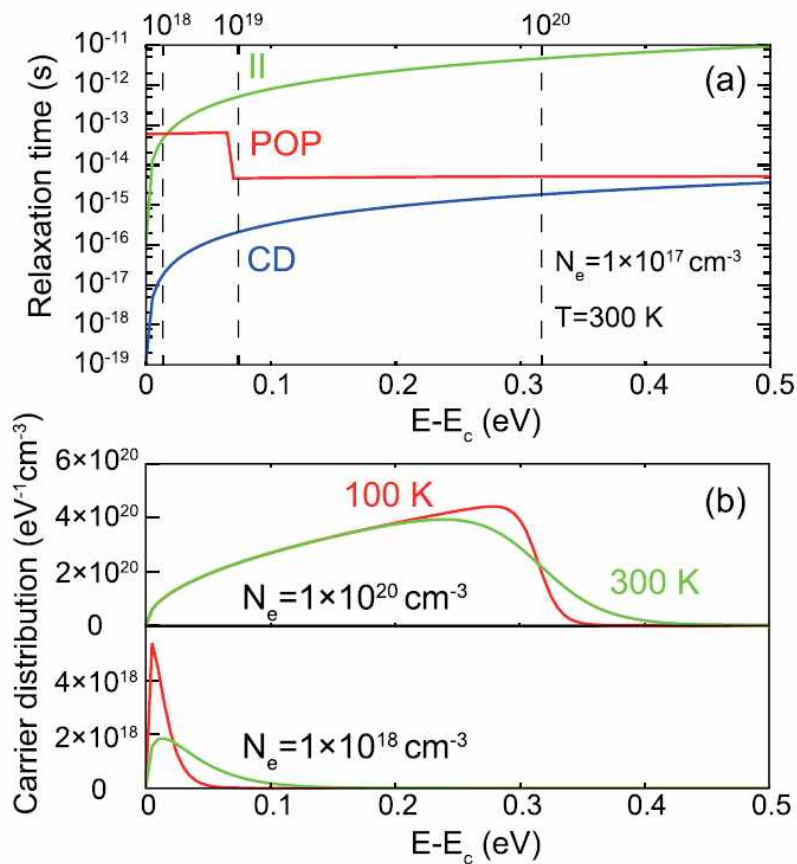


Figure 3.9. (a) The relaxation time for each scattering mechanism with respect to the electron energy relative to the conduction band minimum. The vertical dashed lines represent Fermi levels at 0 K for several carrier densities. (b) Carrier distribution over the electron energy.[28]

3.3.4 Hydrogen defect in In-Zn-Sn-O (IZTO)

In addition to the carrier mobility, improving the stability of OS-based TFT under various stress conditions has been a critical issue to commercialize it.[31-33] Several types of defects in OSs like oxygen vacancy have been suggested as the origin of the instability problems found in experiments,[34,35] but there is no clear explanation. Recently, hydrogen impurity has been received great attentions as the unintentional source of n-type conductivity and PPC in OSs[36-38] because they are easily incorporated into OSs during the device fabrication. Therefore, in this study, we identify the role of hydrogen impurity in amorphous IZTO (a-IZTO) in terms of the device instability. Even though the characteristic atomic sites are not well defined in amorphous materials due to the lack of the periodicity, we classify the hydrogen impurities into 4 categories: H_i^+ , H_i^- , H_o^+ , and $H-DX^-$. H_i refers to the interstitial hydrogen which indicates additional hydrogen atom in a empty space of stoichiometric supercell. H_i can be more divided into two types with respect to their charge states, H_i^+ and H_i^- , because they can exist as cation/anion in a host material. The atomic configuration shows difference between H_i^+ and H_i^- due to the electrostatic potential they create. While H_i^+ makes a bond with O^{2-} ion, H_i^- is surrounded by the metal ions as shown in Fig. 3.10(a) and (b).[39]

H_o^+ and $H-DX^-$ represent the substitutional impurity of the oxygen ions which exhibit positive and negative charge states, respectively.

Interestingly, their atomic configurations which are bonded with metals do not show notable difference as shown in Fig. 3.10(c) and (d), but they can have different charge states due to the distinct orbital hybridization and Madelung potential at the hydrogen sites. In this study, we consider 9, 10, 9 and 6 atomic configurations of H_i^+ , H_i^- , H_o^+ , and $H-DX^-$, respectively, for the statistical analysis.

The anionic nature of the hydrogen impurity can be confirmed by the charge density distribution of Fermi level. It is noted that the charge density diagrams of Fermi level for the supercell with H_i^- and $H-DX^-$ show the localized nature near the hydrogen sites as shown in Fig. 3.11(a) and (b). In contrast, cationic hydrogen states are not found between the band gap because they exist above the conduction band of the host material.

The averaged optical transition energy from the defect states to the conduction band are presented in Fig. 3.11(c) for H_i^- and $H-DX^-$. The width of the given energy levels in blue and red show the standard deviation. The $H-DX^-$ exhibits the optical excitation energy of 1.45 eV in average which is smaller than 2.45 eV of H_i^- implying that $H-DX^-$ is more active for the low energy stress like illumination with low frequency or the thermal excitation. The thermal stability of the hydrogen impurities is assessed by the formation energy calculation in Eq. 2.24. Since the band gap of the GGA+ U calculation is underestimated, we applied the quasiparticle (QP) shift of both valence band maximum (VBM) and conduction band maximum (CBM) following the GW_0 calculation results for binary oxides.[40]

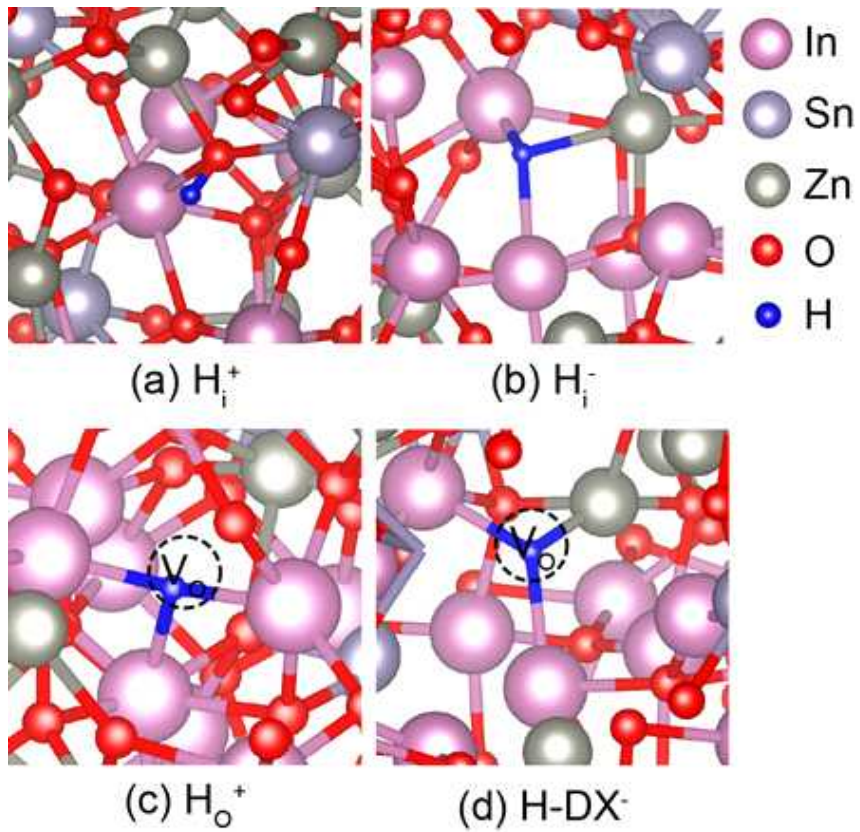


Figure 3.10. Atomic configurations of (a) H_i^+ , (b) H_i^- , (c) H_o^+ , and (d) $H-DX^-$ in a-IZTO host material.[39]

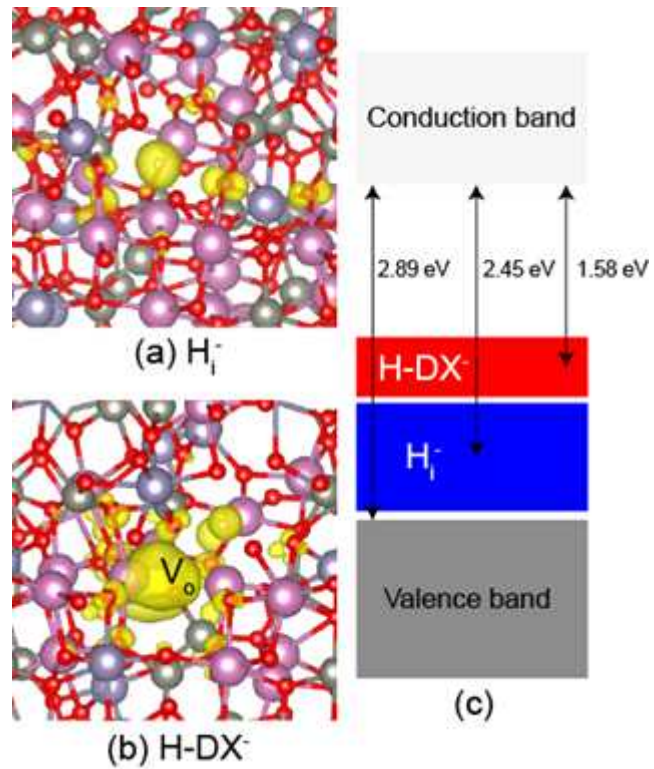


Figure 3.11. Charge densities of (a) H_i^- and (b) $H-DX^-$ states. (c) The schematic diagram of the energy levels of the anionic hydrogen impurities. [39]

To be specific, considering the difference of the experimental (3.19 eV) and GGA+ U (1.39 eV) optical band gap, the QP shifts for VBM and CBM are determined as -0.48 and 1.41 eV, respectively. The chemical potentials of oxygen and hydrogen are obtained by a half of their molecular energies.

Figure 3.12 shows the formation energies for all kinds of hydrogen impurity. The blue and red lines represent of the average formation energies for cationic and anionic hydrogen impurities, respectively, and the dashed lines are the standard deviation. The average transition levels, $\varepsilon(+/-)_{av}$, between + and - charge states are also presented as vertical green line. $\varepsilon(+/-)_{av}$ s from H_i^+ (H_O^+) to H_i^- ($H-DX^-$) are 2.79 (2.96) eV above the VBM.

It is noted that cationic hydrogen impurities are more stable than their anionic counterparts in most regions of Fermi level implying that the hydrogen can be one of the n-type source in OSs.[36-38] On the other hand, the formation energy difference between two charge states is reduced when the E_F approaches CBM indicating the coexist of the two charge states in the n-type a-IZTO.

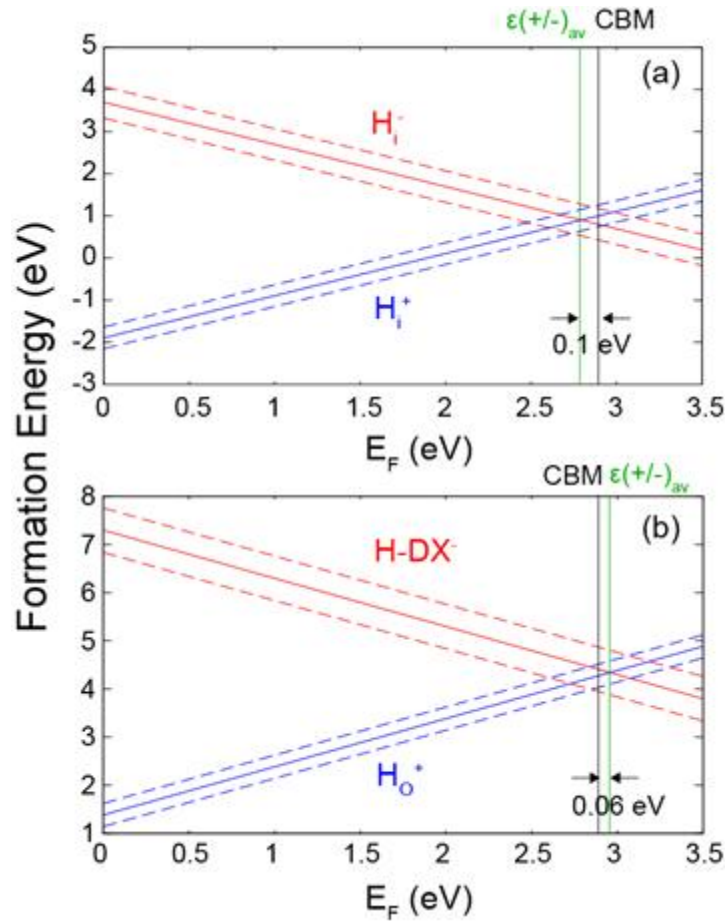


Figure 3.12. Averaged defect formation energies of (a) H_i^+ (blue), H_i^- (red), (b) H_O^+ (blue), and $H\text{-DX}^-$ (red) as a function of the Fermi level (E_F) under H- and O-rich conditions. Dashed lines represent the standard deviation and green vertical line is the average charge transition level.[39]

The transition energy profile for the structural transformation between two charge states are shown in Fig. 3.13. It is noted that the energy barrier, β , for the transition from H_o^+ to $H-DX^-$ is shown within $0.04 < \beta < 0.81$ eV which is quite smaller than $1.05 < \beta < 2.35$ eV of H_i impurity. Therefore, we can see that the transition of the charge states of H_o defect is more available in comparison with H_i defect. (The same trend is also found for the reverse transition.) In addition, the optical excitation of electrons from the anionic hydrogen sites can lead to the transition to the cationic defect without the barrier.

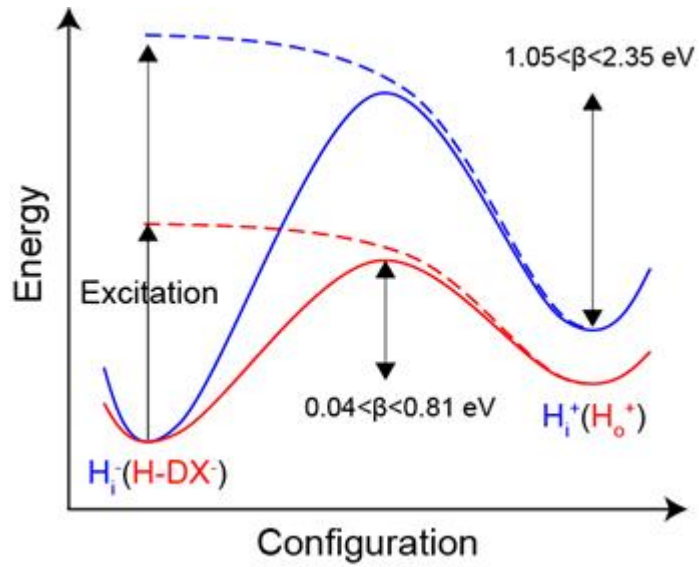
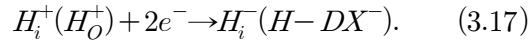
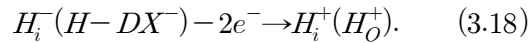


Figure 3.13. Schematic diagrams for the energy with respect to the configurations. The path for the transition between H_i^- and H_i^+ (blue) show higher energy barrier than that between $H-DX^-$ and H_o^+ . [39]

The bistability of hydrogen impurities in terms of their charge states give explanations on the microscopic origin of the negative or positive shifts of the V_{TH} including the speed of the recovery processes under the positive (PBTS) or negative bias thermal stress (NBTS) or illumination stress conditions. As foregoing discussion above, the H_i^+ , H_i^- , H_o^+ , and $H-DX^-$ states can coexist in the a-IZTO sample, relying on the growth condition. The preference of the charge states of the hydrogen impurities can be changed by external stress condition. The PBTS on TFT increases E_F near interface between gate oxide and channel layer causing the following transition in OS channel:



This transition process consumes the free electrons in the conduction band near the channel region shifting the V_{TH} to the positive direction under the PBTS. In the case of the NBTS which lowers E_F , the V_{TH} is shifted to the negative direction due to the charge conversion of



In particular, the illumination further causes the negative V_{TH} shift by accelerating this transition.

Once this transition occur, the recovery process to the original state should be taken place after removing the external stress. Since there are, however, large energy barrier to be overcome for changing the

charge state, it should take quite a long time for the original state before applying bias or illumination stress to be achieved.

3.4. Bibliography

- [1] H.-S. Kim et al., *Sci. Rep.* 3, 1459 (2013).
- [2] T. C. Chen et al., *Thin Solid Films* 520, 1422 (2011).
- [3] B. Ryu et al., *Appl. Phys. Lett.* 97, 022108 (2010).
- [4] K. Nomura et al., *ECS J. Solid State Sci. Technol.* 2, P5 (2013).
- [5] H. J. Kim et al., *J. Phys. D: Appl. Phys.* 46, 055104 (2013).
- [6] I. Souza et al., *Phys. Rev. B* 65, 35109 (2001).
- [7] G. Kresse et al., *Phys. Rev. B* 54, 11169 (1996).
- [8] Y. Kang et al., *Phys. Rev. Lett.* 108, 196404 (2012).
- [9] K. Nomura et al., *Nature* 432, 488 (2004).
- [10] J. Rosen et al., *Phys. Rev. B* 80, 115215 (2009).
- [11] A. Walsh et al., *Chem. Mater.* 21, 5119 (2009).
- [12] T. Kamiya et al., *J. Disp. Technol.* 5, 273 (2009).
- [13] J. C. Smith et al., *Phys. Rev. Lett.* 106, 056401 (2011).
- [14] *Handbook of Transparent Conductors*, edited by D. S. Ginley (Springer, New York, 2011).
- [15] H.-X. Deng et al., *Phys. Rev. B* 87, 125203 (2013).
- [16] J. Robertson et al., *Phys. Stat. Sol. (b)* 245, 1026 (2008).
- [17] J. Batista et al., *Appl. Phys. Lett.* 82, 4077 (2003).
- [18] W. Walukiewicz et al., *J. Appl. Phys.* 50, 899 (1979)..
- [19] T. Makino et al., *Appl. Phys. Lett.* 87, 22101 (2005).
- [20] B. K. Ridley et al., *Quantum Process in Semiconductors* (Oxford University Press, New York, 1993). 3rd ed.

- [21] H. Suzuura et al., Phys. Rev. Lett. 89, 266603 (2002).
- [22] D. Chattopadhyay et al., Rev. Mod. Phys. 53, 745 (1981).
- [23] K. Nomura et al., Nature 432, 488 (2004).
- [24] H. Yabuta et al., Appl. Phys. Lett. 89, 112123 (2006).
- [25] T. Kamiya et al., Sci. Technol. Adv. Mater. 11, 44305 (2010).
- [26] K. Nomura et al., Appl. Phys. Lett. 85, 1993 (2004).
- [27] T. Kamiya et al., J. Disp. Technol. 5, 462 (2009).
- [28] Y. Kang et al., Appl. Phys. Lett. 102, 152104 (2013).
- [29] N. A. Poklonski et al., J. Appl. Phys. 93, 9749 (2003).
- [30] J. L. F. Da Silva et al., Phys. Rev. B 80, 214118 (2009).
- [31] K. Ghaffazadeh et al., Appl. Phys. Lett. 97, 113504 (2010).
- [32] B. S. Yang et al., J. Mater. Chem. 22, 10994 (2012).
- [33] J. Robertson et al., Appl. Phys. Lett. 104, 162102 (2014).
- [34] S. Jeon et al., Nat. Mater. 11, 301 (2012).
- [35] S. Yang et al., Appl. Phys. Lett. 99, 102103 (2011).
- [36] A. Janotti et al., Nat. Mater. 6, 44 (2007).
- [37] J. Ji et al., Appl. Phys. Lett. 105, 041102 (2014).
- [38] H.-H. Nahm et al., Sci. Rep. 4, 4124 (2014).
- [39] Y. Kang et al., Adv. Electron. Mater. 2015, 1400006 (2015).
- [40] Y. Kang et al., Phys. Rev. B 89, 165130 (2014).

4.1 Introduction

In this chapter, the optical properties of OSs are investigated using DFT calculations. It was reported that light illumination on TFT using OSs causes significant shift of V_{TH} under negative gate bias as well as PPC.[1-3] Since such instability problems of OSs are deeply related with atomic and electronic structures, microscopic understanding on the optical properties of OSs is important. In this study, we discuss the technical issues on the band gap calculations within the DFT formalism for the more realistic understanding. In particular, the GW calculation scheme which is state-of-the art method for calculating the electronic structure is dealt with. Finally, the visible light absorption in the amorphous OSs which is one of the problems for the practical use of the OSs is also investigated by evaluating the optical absorption coefficient.

4.2 Calculation method

The various levels of the self-consistency of the GW calculation are tested for ZnO, β -Ga₂O₃, cubic In₂O₃, and rutile SnO₂ in Fig. 4.1.[4] The lattice parameters are fixed to the experimental values and the internal coordinates of the atoms are relaxed within PBE functional. The cutoff energy of 500 eV is used for the plane-wave basis set and the Γ centered k-point meshes are selected as $9 \times 9 \times 7$ (ZnO), $4 \times 4 \times 4$ (Ga₂O₃), $3 \times 3 \times 3$ (In₂O₃), and $5 \times 5 \times 7$ (SnO₂). We use 160 (ZnO), 120 (Ga₂O₃), 576 (In₂O₃), and 160 (SnO₂) bands for calculating the self-energy, which ensure the convergence of the quasiparticle gap within ~ 0.1 eV. For the initial DFT calculations, we use the PBE, GGA+ U , and HSE06 hybrid functionals. The effective U for metal d electrons are given by 7.5, 6.5, 5.0, and 3.5 eV for Zn, Ga, In, and Sn, respectively, and the mixing parameter for HSE06 calculation is fixed to 0.25.

The optical absorption coefficient for amorphous InGaZnO₄ (a-IGZO1) is obtained by the DFT calculation.[5] The atomic structure of a-IGZO1 with 98 atoms is obtained by molecular dynamic (MD) simulation as shown in Fig. 4.2 and ten amorphous structure are generated for the statistical analysis. The MD and relaxation steps are performed using PBEsol functional.[6] To overcome the band gap underestimation of the PBE functional, the quasiparticle shifts within GW_0 calculation on the basis of GGA+ U calculation are employed. The plane-wave basis cutoff

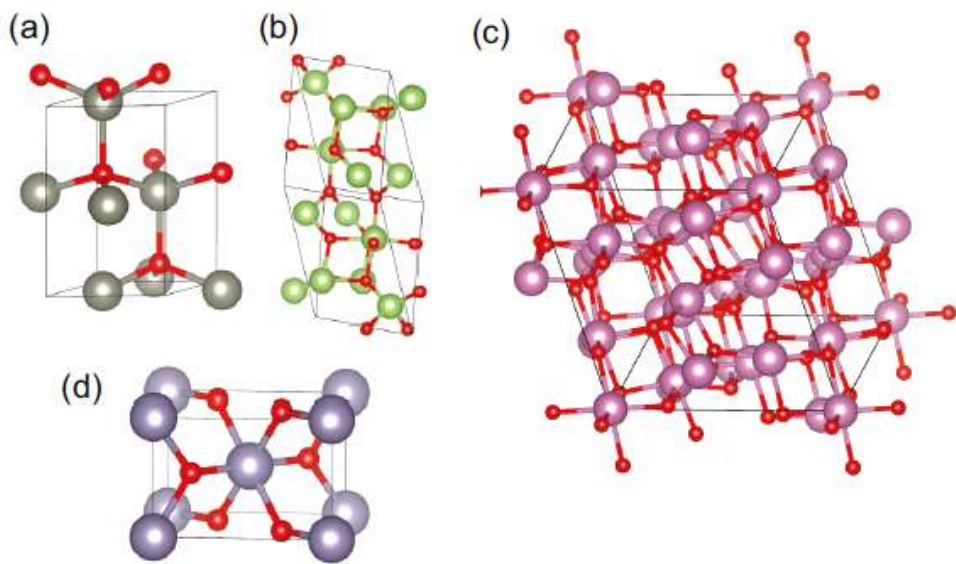


Figure 4.1. The unitcells of (a) wurtzite ZnO, (b) β -Ga₂O₃, (c) bixbite In₂O₃, and (d) rutile SnO₂. The small red balls are oxygens and other ones are metals.[4]

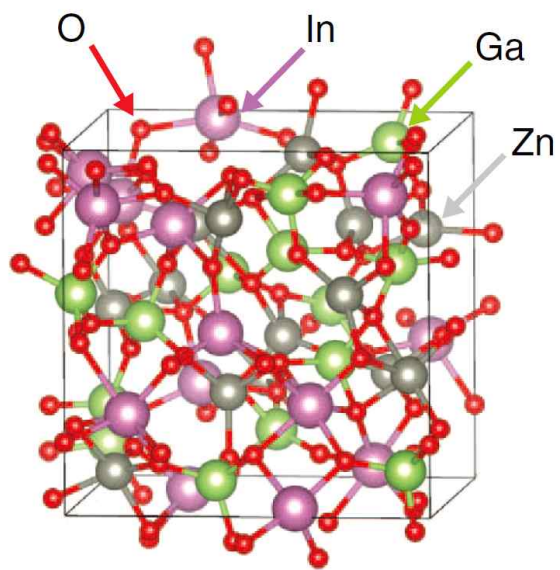


Figure 4.2. The amorphous structure of a-IGZO.[5]

of 500 eV is used and the total number of the bands and k-point mesh for evaluating self-energy in GW_0 calculation are 1152 and Γ centered $2 \times 2 \times 2$, respectively. All the above DFT and GW calculations are performed by VASP code.[7]

4.3 Result and discussion

4.3.1 Band gap of OS in GW approximation

Presently, the GW calculation is implemented within RPA which gives the dielectric constants with fair accuracy based on the DFT calculation.[8] This is because the error cancelation between the RPA and the small band gap. If we apply the fully self-consistent GW calculation (QPGW), it usually overestimate the band gap due to the reduction of the dielectric function during the self-consistent iteration.[5] Therefore, we rely on the W_0 scheme where the dielectric constant is maintained as that of the DFT calculation.

Since the GW calculation results depend on the initial DFT calculation, we tested GGA, GGA+ U , and HSE06 functional. Even though the self-energy of the GW calculation is obtained considering full frequency dependent dielectric function, its static part of the dielectric constant corresponding to that of $\omega=0$ can be one of the most important criterions for identification of an appropriate initial DFT calculation.[9]

Figure 4.3 shows that the static dielectric constant of the GGA(HSE06) is over(under)estimated in comparison with experimental value and GGA+ U results in the smallest error among them within RPA. The large error of GGA is on the contrary to the calculation results of the conventional sp semiconductors or insulators such as Si and Ge where the GGA estimates dielectric constant with fair accuracy within RPA.

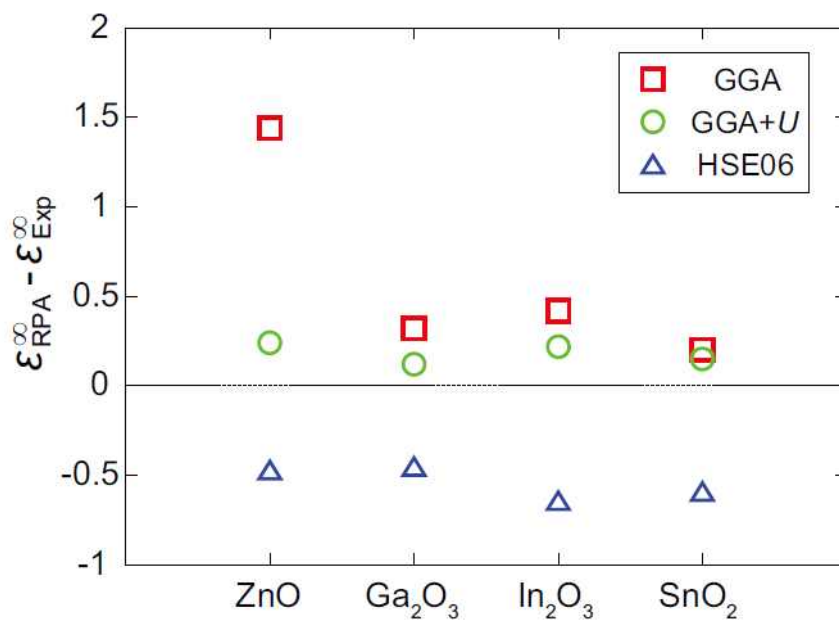


Figure. 4.3. Difference between theoretical and experimental optical dielectric constants, ϵ_{RPA}^{∞} and ϵ_{Exp}^{∞} . [4,12,14-16]

The main reason of large error of the GGA functional for OSs is more severe underestimation of the band gap of the GGA method due to the shallow metal- d band positions that further reduces the band gap by the repulsion between metal- d and oxygen- p bands.[10,11] This can be partially cured by applying GGA+ U functional which lowers the metal- d bands energy, and therefore, slightly increases the band gaps by weakening the p - d repulsion. As a results, the GGA+ U calculations of OSs reduces the error of dielectric constants between calculation (within RPA) and experiments. Whereas, the HSE06 functional itself more opens the band gaps leading to the underestimation of the dielectric constant within RPA. Thus, we select the GGA+ U functional as the initial DFT calculations for the W_0 .

We compare the various GW band gaps and the experimental values in Fig. 4.4. The HSE06 based G_0W_0 calculation results ($G_0W_0@HSE06$) is also provided for the comparison since it is often employed in previous literatures.[12-14] The GGA+ U functional gives the larger band gap than the GGA functional, but it still underestimates the band gaps of the experiments severely. The G_0W_0 one-shot calculation greatly improves the results of the GGA+ U and the mean absolute residual error (MARE) of the G_0W_0 calculations is 12.33%. However, there is systematic underestimation of the G_0W_0 band gap. If eigenvalues are updated within GW_0 calculation, the band gaps more increases in comparison with G_0W_0 calculation reducing the error and MARE of GW_0 calculations up to 5.49%. When we update the wavefunction additionally within QPGW $_0$ calculation, the band gaps become larger than

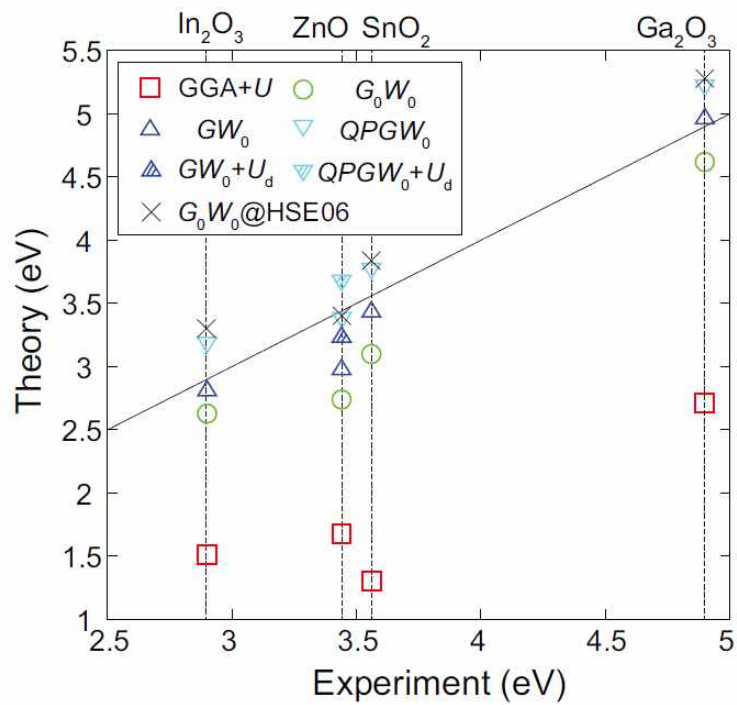


Figure 4.4. The band gaps evaluated by various computational methods are plotted with respect to experimental data.[4]

those of GW_0 calculations leading to the overestimation of the band gap with MARE of 5.66%. The only exception of the overestimation of the QPGW_0 is the ZnO, but the Zn- d still remains too shallow in comparison with experimental result and we will further discuss it in the below. Interestingly, the $\text{G}_0\text{W}_0@HSE06$ calculation shows similar band gaps of the QPGW_0 as shown in Table. 4.1.

We emphasized the importance of the optical dielectric constant for W_0 scheme. To explicitly examine this, we performed GW_0 calculations based on GGA, $\text{GGA}+U$, and HSE06. Figure 4.5 shows that the GW_0 band gaps of the tested materials increases in the order of the GGA, $\text{GGA}+U$, and HSE06. Even though there are various theoretical origins to give different band gaps, the results in Fig. 4.5 underlines the importance of the dielectric constant for the GW_0 calculations.

On the other hand, the band gap of the ZnO is still underestimated by ~ 0.5 eV in GW_0 calculation in contrast to the others. This is because GW method still suffer from the self-interaction error[17] causing that the Zn- d band is located close to the valence band maximum of the oxygen p bands. Therefore, the lower binding energy of the Zn- d electrons in GW_0 calculation does not fix the p - d repulsion completely leading to the smaller band gaps. To address this, we introduce additional on-site energy U_d . The value was selected for the d band positions in GW_0+U_d calculation to lie within 0.1 eV of the experimental data and its value is 3.0 eV for Zn- d electron. If we

Table 4.1. The calculated band gaps (in eV) of the various binary OSs. The values in parentheses are obtained by GW_0+U_d calculations.[4]

| | GGA + U | G_0W_0 | GW_0 | $QPGW_0$ | G_0W_0 @HSE06 | Expt. |
|--------------------------------|-----------|-------------|-------------|-------------|-----------------|-------------------|
| ZnO | 1.68 | 2.74 (2.95) | 2.97 (3.24) | 3.39 (3.70) | 3.22 | 3.44 ^a |
| Ga ₂ O ₃ | 2.71 | 4.62 | 4.96 | 5.23 | 5.30 | 4.90 ^b |
| In ₂ O ₃ | 1.51 | 2.60 | 2.80 | 3.14 | 3.35 | 2.90 ^c |
| SnO ₂ | 1.30 | 3.10 | 3.43 | 3.78 | 3.89 | 3.56 ^d |

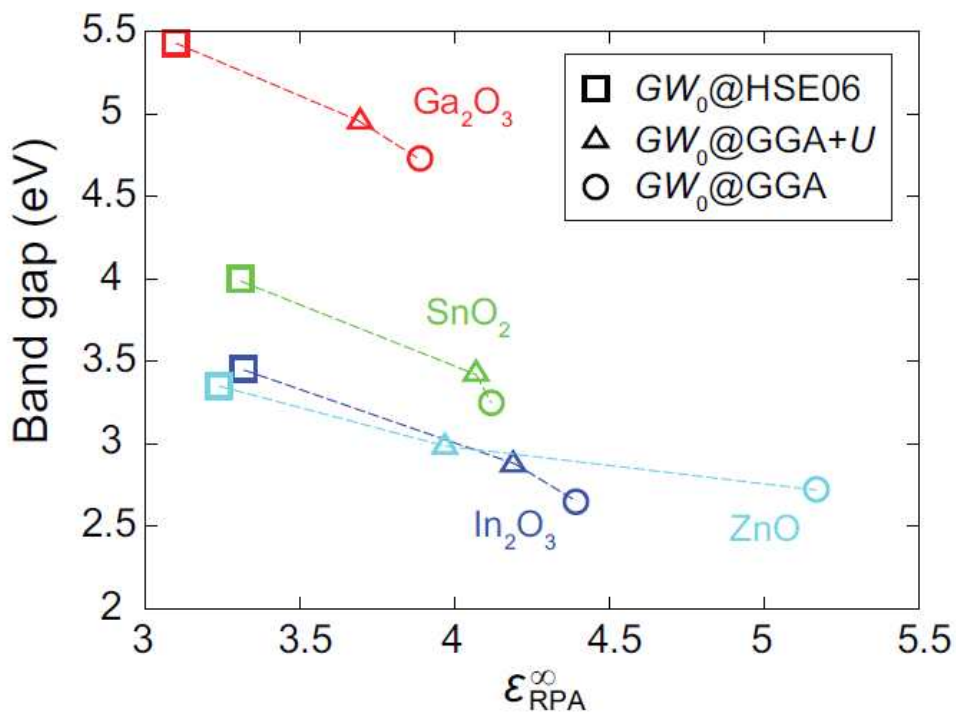


Figure 4.5. The GW_0 band gaps obtained by different initial functionals shown as a function of optical dielectric constant of the calculation.[4]

apply GW_0+U_d scheme to ZnO, the agreement of GW_0 calculation and experiments is quite improved showing the MARE of 3.53%. (The effect of the U_d for other OSs is insignificant due to the relatively large separation of the metal d band from the oxygen p bands.)

The fundamental band gap of In_2O_3 has been an issue; the various experimental band gaps from 2.62 to 3.75 eV have been reported.[18-20] Recently, the GGA+ U calculations with x-ray measurements proposed the band gap of In_2O_3 is 2.9 eV and the larger band gap than 3.5 eV is a results of the forbidden transition in optical absorption experiments. Our GW_0 calculation also yields 2.80 eV as the minimum band gap supporting the results in Ref. 20.

Finally, we confirm whether the present method is still valid or not for the compound OSs. To test this, the band gaps of the crystalline InGaZnO_4 is calculated using GW_0+U_d method with same on-site energies of the binary OSs. For GW calculations, we employed $7\times 7\times 1$ k-points and 288 bands to evaluate the self-energy. It revealed that the quasiparticle gap is 3.74 eV which shows good agreement with experimental band gap of 3.7 eV.[21]

4.3.2 Optical absorption of crystalline and amorphous IGZO

The visible light absorption of OSs has been issues related with the instability problems of the TFT using OSs. In this chapter, we discuss the intrinsic optical absorption of the stoichiometric InGaZnO₄ in amorphous phase (a-IGZO). To correct the band gap underestimation of the conventional DFT calculations, we performed the GW₀ calculations for five a-IGZOs on the basis of GGA+*U* calculations. Figure 4.6(a) shows the quasiparticle levels (ϵ^{QP}) with respect to GGA+*U* energies (ϵ^{DFT}) and it is found that there is linear relation between ϵ^{DFT} and ϵ^{QP} approximately:[5,22,23]

$$\epsilon_{v(c)}^{QP} = a_{v(c)}\epsilon_{v(c)}^{DFT} + \Delta_{v(c)}, \quad (4.1)$$

where $\epsilon_{v(c)}^{QP}$ is the quasiparticle levels of valence(conduction) bands. Based on this linear relation, the density of states (DOS) of the GGA+*U* (D^{DFT}) which is averaged over ten a-IGZOs is rescaled (D^{GW}) as follows:

$$D_{v(c)}^{GW}(E) \cong \frac{1}{a_{v(c)}} D_{v(c)}^{DFT}\left(\frac{E - \Delta_{v(c)}}{a_{v(c)}}\right). \quad (4.2)$$

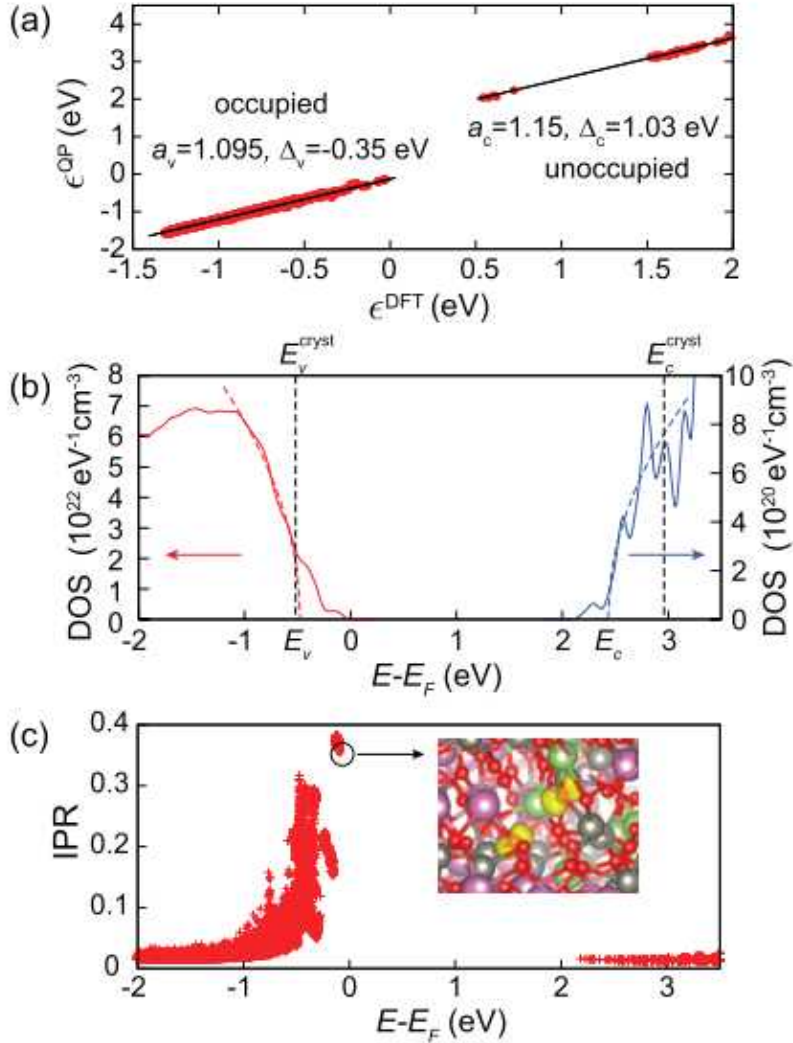


Figure 4.6. (a) The ϵ^{QP} s with respect to the ϵ^{DFT} s of GGA+U calculations. The linear lines represent fitted results. (b) The averaged DOS of a-IGZO which is rescaled by quasiparticle shift in (a). The vertical dashed lines show the band edges in c-IGZO. (c) The inverse-participation ratio (IPR) for each electronic state. The inset is the charge density of the state at the Fermi level.[5]

Figure 4.6(b) shows the D^{GW} obtained by Eq. 4.2.

The localization of the electronic states is examined by the inverse participation ratio (IPR)[24] and it is noted that the valence band states between the band edge and ~ -0.5 eV are strongly localized as shown in Fig. 4.6(c). In contrast to the valence band states, the wave function of the conduction states broadly spread over the whole atomic sites. This is because the valence band states mainly consist of the oxygen p orbitals which are easily localized by the structural disorder due to its directionality while the spherical metal s orbitals mainly forms the conduction band states.[25]

To explicitly determine the band edges, we fit the DOS using the equation of $D_{v(c)} \propto \sqrt{|E_{v(c)} - E|}$, where $E_{v(c)}$ represents the mobility edges which separates the localized tail states from the extended states. The dashed curves in Fig. 4.6(b) represent the fitting curves and it is found that E_v and E_c are located -0.53 and 2.38 eV with respect to Fermi level implying that the widths of the tail states of the valence and conduction bands are ~ 0.5 and ~ 0.1 eV. We also provide the band edge positions of the crystalline IGZO (c-IGZO) as $E_{v(c)}^{cryst}$ by aligning the oxygen $1s$ levels between a- and c-IGZO (see dashed vertical lines in Fig. 4.6(b)).[26] It is noted that E_v of a-IGZO is ~ 0.05 eV higher than E_v^{cryst} while E_c is 0.55 eV lower than E_c^{cryst} . The large down-shift of the conduction band in a-IGZO is also observed in XPS measurement showing E_v (E_c) is higher(lower) than for c-IGZO by 0.1 (0.48) eV.[27,28]

To reveal the microscopic origin of the significant reduction of E_c in a-IGZO, we examine the core potentials (V_{core}) at the metal sites because the main component of the conduction bottom is metal s orbitals. The potential difference between a-IGZO and c-IGZO, $\Delta V_{core} (= V_{core}^{amor} - V_{core}^{cryst})$, is computed and the partial weight of the metals on the conduction bottom with respect to ΔV_{core} is plotted in Fig. 4.7(a). It is found that the wave function of the conduction state is mainly distributed on In sites with lower electrostatic potential. In addition, ΔV_{core} against the coordination number (CN) is shown in Fig. 4.7(b) and the linear relation is found between ΔV_{core} and CN implying ΔV_{core} increases with CN. It can be understood by considering the neighboring ions around metal ions are the oxygen with 2- charge state which offer the negative potential to the neighboring metal sites. Since the CN is fluctuated over whole metal sites in a-IGZO, certain In site can have lower CN than other sites. In addition, the average CN of In in a-IGZO is reduced to 5.58 in comparison with 6.00 in c-IGZO which more critically lowers the potential at In sites leading to the large down-shift of the conduction band.

By reflecting above calculation results of DOS in a-IGZO, the optical absorption constant (α) is evaluated. Because $\varepsilon_2/\varepsilon_1 \ll 1$ for the transition near band edges, Eq. 2.27 can be approximately reduced to[29]

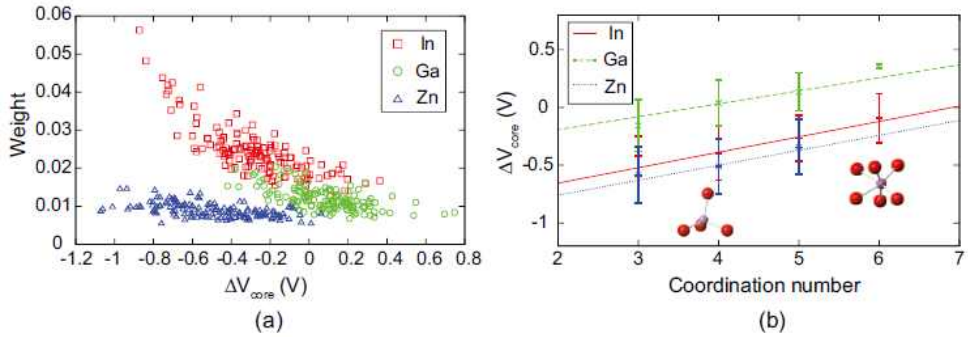


Figure 4.7. (a) The projected partial weight of the conduction bottom on each cation as a function of the core potential difference, ΔV_{core} , between a- and c-IGZO. (b) The ΔV_{core} plotted with respect to the coordination number (CN). The straight lines are the linear regression results and the insets indicate In atoms with different CNs.[5]

$$\alpha(E_{ph}) \simeq \frac{E_{ph}}{\hbar c} \frac{\mu}{\sqrt{\varepsilon_1(0)}} JDOS(E_{ph}), \quad (4.3)$$

where $JDOS$ is joint density-of-states which is defined as

$$JDOS(E) = \int D_v(E') D_c(E' + E) dE'. \quad (4.3)$$

μ in Eq. 4.3 represents the ratio of ε_2 to $JDOS$ for the band edge transition and it is obtained by averaging ε_2 and $JDOS$ over the all a-IGZO structures.

The optical absorption spectrum is presented in the form of Tauc relation $\{(\alpha E_{ph})^{1/2}\}$ in Fig. 4.4(a). The optical band gap (E_g^{opt}) is given as the extrapolated intercept of linear region with x-axis (see dashed lines). The theoretical E_g^{opt} is 2.82 eV, which is in good agreement with experimental value of 3.05 eV.[30] Furthermore, we also provide E_g^{opt} of c-IGZO and it is given by 3.57 eV which is comparable with experimental value of 3.70 eV.[21]

Even though there is still discrepancy of 0.23 eV in E_g^{opt} of a-IGZO between calculation and experiment, our calculation well reproduces the experimental absorption spectrum from E_g^{opt} to $E_g^{opt}-0.4$ eV. Therefore, we can see that the intrinsic tail states near valence band edge and the large down-shift of the conduction band in a-IGZO are responsible for the visible light absorption above the blue region (≥ 2.6 eV in experiments). Figure 4.4(b) shows a schematic diagram for the different

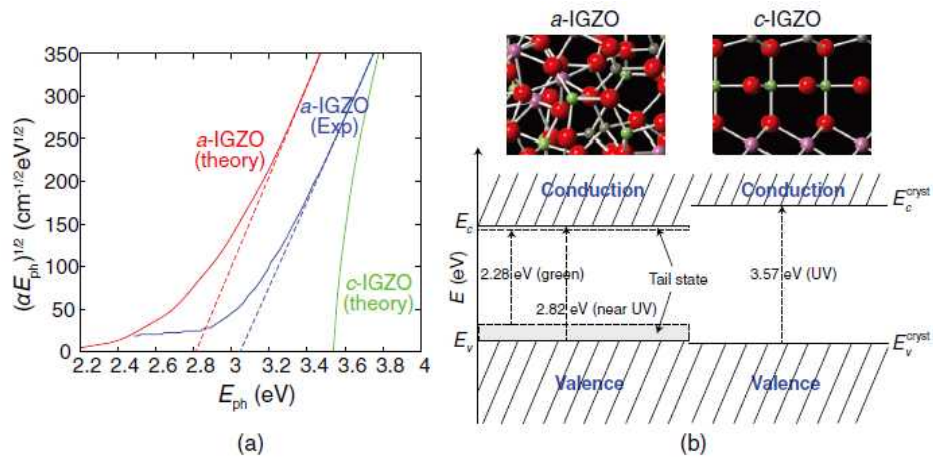


Figure 4.8. (a) Tauc plots for optical absorptions in c- and a-IGZO evaluated by Eq. 4.3. (b) Schematic figures showing the electronic structures and distinct absorption behavior of c- and a-IGZO.[2]

optical absorption between in c- and a-IGZO. Because the serious light instability in a-IGZO arise mainly from the illumination of the light with higher energy than blue,[30] we pay attention to the peroxide formation mechanism in Ref. 31.

4.4 Bibliography

- [1] S. Jeon et al., *Nat. Mater.* 11, 301 (2012).
- [2] M. D. H. Chowdhury et al., *Appl. Phys. Lett.* 97, 173506 (2010).
- [3] P. Gorrn et al., *Appl. Phys. Lett.* 91, 193504 (2007).
- [4] Y. Kang et al., *Phys. Rev. B* 89, 165130 (2014).
- [5] Y. Kang et al., *APL Materials* 2, 32108 (2014).
- [6] J. P. Perdew et al., *Phys. Rev. Lett.* 100, 136406 (2008).
- [7] G. Kresee et al., *Phys. Rev. B* 54, 11169 (1996).
- [8] M. Shishkin et al., *Phys. Rev. Lett.* 99, 246403 (2007).
- [9] M. Shishkin et al., *Phys. Rev. B* 75, 235102 (2007).
- [10] H. K. Noh et al., *Phys. Rev. B* 84, 115205 (2011).
- [11] A. Janotti et al., *Appl. Phys. Lett.* 87, 122102 (2005).
- [12] A. Schleife et al., *Phys. Rev. B* 83, 035116 (2011).
- [13] B. Hoffling et al., *Phys. Rev. B* 85, 035305 (2012).
- [14] F. Fuchs et al., *Phys. Rev. B* 77, 155107 (2008).
- [15] N. Ashkenov et al., *J. Appl. Phys.* 93, 126 (2003).
- [16] M. Rebien et al., *Appl. Phys. Lett.* 81, 250 (2002).
- [17] W. Nelson et al., *Phys. Rev. A* 75, 32505 (2007).
- [18] A. Klein et al., *Appl. Phys. Lett.* 77, 2009 (2000).
- [19] P. Erhart et al., *Phys. Rev. B* 75, 153205 (2007).
- [20] A. Walsh et al., *Phys. Rev. Lett.* 100, 167402 (2008).
- [21] T. Kamiya et al., *J. Disp. Technol.* 5, 273 (2009).
- [22] M. Rohlfiing et al., *Phys. Rev. B* 62, 4927 (2000).
- [23] S. Sharifzadeh et al., *Phys. Rev. B* 85, 125307 (2012).

- [24] E. Cho et al., J. Appl. Phys. 109, 043705 (2011).
- [25] Y. Kang et al., Phys. Rev. Lett. 108, 196404 (2012).
- [26] L. E. Hintzsche et al., Phys. Rev. B 86, 235204 (2012).
- [27] K. Lee et al., J. Appl. Phys. 112, 33713 (2012).
- [28] Y. Kang et al., J. Mater. Chem. C 2, 9196 (2014).
- [29] B. Sadigh et al., Phys. Rev. Lett. 106, 027401 (2011).
- [30] C.-S. Chuang et al., SID Int. Symp. Dig. Tech. Pap. 39, 1215 (2008).
- [31] H. -H. Nahm et al., Phys. Status Solidi B 249, 1277 (2012).

CHAPTER 5

Conclusion

In this study, we investigate the optical and electrical properties of OSs which consists of metal with d^0 configuration like In, Ga, Zn, and Sn and oxygen. Since they provide the high carrier mobility in amorphous phase, the low temperature fabrication of the opto-electronic device using OSs is possible, which has attracted tremendous industrial interests. In spite of highly fascinating advantages of OSs, the realization of the commercial device is still limited and further improvement of carrier mobility of OSs and device instability is highly required. The purpose of this study is to extend the understanding of the various phenomenons and properties in atomic levels on the basis of the quantum simulations in order to efficiently achieve enhancement of performance of the device in terms of the speed and the stability.

We provide theoretical framework to understand the distinctive transport behavior in OSs. Our TB model reveals that the quasi-linear conduction bands arise in OSs due to the parallel and isotropic coupling between metal s and oxygen p orbitals which does not depend on the orientational disorder of the polyhedra around metal and oxygen in atomic structure. As a result, the dispersive conduction band of amorphous OSs can be preserved in contrast to Si and GaAs implying that the reduction of the electron mobility in amorphous OS does not

occur.

The quasi-linear band structure strongly influences on the transport properties in OSs for the highly doped samples. The electron mobility in ZnO shows upshift at 10^{19} cm^{-3} of carrier concentration in spite of increasing the ionic impurity scattering. This abnormal behavior can be explained by the back scattering suppression due to the linear relation of the conduction band structure.

On the other hand, the experimental results that the electron mobility in compound semiconductors like IGZO is enhanced with the carrier density and temperature are explained by the cation disorder (CD) scattering. To evaluate the scattering rate of the electrons in c-IGZO, we introduce the virtual crystal approximation. In this approach, the random distribution of Ga and Zn is treated as the scattering center. The CD provides the dominant scattering source in comparison with other scattering mechanisms like ionized impurity and polar optical phonon. Since the relaxation time for CD scattering increase with the electron energy which gives an explanation of the carrier concentration and temperature dependence of electron mobility.

Previous experimental researches showed various instability problems of OS based TFT and they suggested the defects like oxygen vacancy as the origin of such problems. In this study, we investigate the behavior of the hydrogen impurity in OSs which is accepted as quasi-intrinsic impurity due to its abundance in the air. The total energy calculations based on the DFT reveals that the hydrogen impurity shows bistability in terms of the charge states. Since the

hydrogen can exist as cation or anion depending on the Fermi level, the TFT using OSs undergoes the threshold shift under gate bias and illumination stress.

Finally, to assess the optical property, we carry out the GW calculation which provides the accurate band gap of OSs. The electronic density of state (DOS) of a-IGZO is modified by using the GW calculation results and based on its DOS we calculate the optical absorption spectrum. Our calculated absorption spectrum shows good agreement with experimental data. It is found that the long tail states near valence band edge and the down-shift of the conduction bottom in a-IGZO relative to c-IGZO is the origin of the visible light absorption with more than 2.6 eV corresponding to blue light. Therefore, we consider the peroxide formation mechanism in a-IGZO as a intrinsic origin of device instability and PPC.

In conclusion, using *ab-initio* calculation methods, we extend our physical insights into the optical and electrical properties of OSs in terms of carrier mobility and device stability. However, various scientific and engineering issues on OSs still remains unresolved. For example, microscopic origin of PPC in crystalline OSs like ZnO and In_2O_3 is not obvious, which hinders to develop the efficient UV sensor using OSs. In addition, even though many attempts to introduce hole carrier into OSs have been tried, the successful p-type doping which can endow more functionality to OSs has not been reported. Therefore, we further investigate such unresolved problems related with OSs to widen the applicability using *ab-initio* calculation.

국문초록

최근 저온 공정을 통해 제작한 산화물 반도체 박막 트랜지스터가 좋은 성능을 보임에 따라 이를 차세대 디스플레이에 활용하기 위한 연구가 활발히 이루어지고 있다. 산화물 반도체는 기존의 비정질 실리콘 반도체에 비해 이동도가 10배 이상 높고 저온 공정이 가능하다는 특성 때문에 유연 소자 제작이 가능하다. 따라서, 대면적 고해상도 유연성 디스플레이 제작을 위한 산화물 반도체 기반 트랜지스터 개발이 세계적인 큰 관심사이다.

산화물 반도체는 여러 장점에도 불구하고, 실용화를 위해서는 여러 가지 장애물을 극복해야 한다. 먼저, 산화물 반도체의 전자의 이동도는 $\sim 10 \text{ cm}^2/\text{Vs}$ 이지만 실제 고해상도 디스플레이 제작을 위해서는 $20 \text{ cm}^2/\text{Vs}$ 이상의 이동도를 필요로 한다. 따라서, 산화물 반도체에서의 전자의 이동도를 증가시키는 방안을 찾는 것이 중요하다고 할 수 있다.

또한, 여러 실험에서 밝혀졌듯이, 산화물 반도체 기반 트랜지스터는 외부 빛 또는 게이트 전압을 장시간 인가하였을 때 소자의 성능이 크게 바뀌는 현상이 나타난다. 이러한 산화물 반도체의 비 안정성 문제에 대해 다양한 원인들이 제시되었지만 여전히 이를 해결하기 위한 노력이 필요한 실정이다.

본 연구에서는 먼저 산화물 반도체 내부에서 전자가 어떠한 거동을 보이는지, 나아가 전자의 이동도가 어떻게 결정되는지에 대해 이론적 연구를 진행하였다. 특히 비정질 산화물 반도체에서 전자가 결정질 물질과 같이 빨리 움직일 수 있는 원인을 찾아내고 이를 통해 산화물 반도체의 전자 이동도를 증가시킬 수 있는 방안을 찾아보고자 하였다. 또한 다양

한 전자 산란 메커니즘을 통해 직접 전자의 이동도를 계산함으로써 산화물 반도체의 전자 이동도가 어떻게 결정될 수 있는지에 대해 알아보았다.

또한 산화물 반도체의 불안정성을 야기시킬 수 있는 수소 결함에 대한 연구를 진행하였다. 수소는 소자 제작시 언제든지 산화물 반도체 내부로 들어갈 수 있는 원소로서, 수소가 +1/-1의 두가지 전자 상태를 가질 수 있음을 밝혀내었고 이러한 수소의 특성으로 인해 소자의 불안정성이 커질 수 있음에 대해 논의 하였다.

마지막으로 산화물 반도체의 광학적 성질을 이론적으로 분석함을 통해 빛으로 인한 산화물 반도체의 불안정성의 원인을 찾아 보고자 하였다. 본 연구에서는 비정질 산화물 반도체의 원자구조를 먼저 모델링 한 후 결정질 산화물 반도체와의 차이를 비교 분석하였는데, 이를 통해 비정질 산화물 반도체는 광학적 밴드갭이 줄어들고 valence band 근처에 긴 tail state들이 발생한다는 것을 밝혔다. 결국 갭의 줄어듦과 긴 tail state는 외부에서 들어오는 가시광 및 UV 빛에 대해 반응하여 산화물 반도체의 특성이 바뀔 수 있음을 보여주었다.

Keywords : 산화물 반도체, 범밀도함수이론, 전자수송, 점 결함, 빛 흡수도

Student Number : 2011-20616